IMRT DOSE VERIFICATION WITH ELECTRONIC PORTAL IMAGERS

A STUDY OF IMRT PRE-TREATMENT DOSE VERIFICATION USING A-SI ELECTRONIC PORTAL IMAGING DEVICES

By ELEODOR NICHITA, B.SC., M.SC., PH.D.

A Thesis Submitted to the School of Graduate Studies in Partial Fulfilment of the Requirements for the Degree Master of Science

McMaster University

MASTER OF SCIENCE (2012)

Hamilton, Ontario

TITLE: A Study of IMRT Pre-Treatment Dose Verification Using a-Si Electronic Portal Imaging Devices

AUTHOR: Eleodor Nichita, B.Sc., M.Sc., Ph.D

SUPERVISOR: Dr. O.Z. Ostapiak

NUMBER OF PAGES: xii, 64

Abstract

Intensity-Modulated Radiation Treatment (IMRT) requires patient-specific quality assurance measurements, which can benefit from the convenience of using an Electronic Portal Imaging Device (EPID) for dose verification. However, EPIDs have limitations stemming from the non-uniform backscatter due to the support-arm as well as from scatter, glare, and an increased sensitivity to low-energy photons. None of these effects is typically accounted for in a treatment planning system (TPS) model, resulting in errors in calculated EPID response of up to 6%. This work addresses the non-uniform backscatter by directly incorporating a support-arm backscatter region into the TPS geometry. The shape of the backscatter region is adjusted iteratively until the TPS-calculated flood-field planar dose matches the flood-field EPID image The scatter, glare and increased low-energy response are addressed by using a radially-dependent Point-Spread Function (Kernel). The kernel is fitted using a least-squares method so that it best reproduces the EPID-acquired image for a checkerboard field. The backscatter-correction method is implemented for a Varian Clinac equipped with a 40 cm x 30 cm (512 x 384 pixel) EPID and a Pinnacle^3 TPS and tested for several rectangular and IMRT fields. The scatter, glare and energy-response correction kernel is implemented and tested for a simulated checkerboard field and a simulated IMRT field. Agreement between the EPID-measured image and TPS-calculated planar dose map is seen to improve from 6% to 2% when the backscatter region is added to the Pinnacle^3 model. Agreement between the simulated EPID images and simulated TPS images is improved from 14% to approx. 1% when the radially-dependent kernel is used. Simultaneous application of both the backscatter region and Point-Spread Function is a promising direction for future investigations.

Acknowledgments

I would like to express my appreciation to my thesis supervisor, Dr. Orest Ostapiak, for his guidance and patience during the course of this work. I would also like to thank Dr. Tom Farrell for useful advice and suggestions. Finally, I would like to acknowledge all the physicists, technologists, residents, IT specialists and fellow students at the Juravinski Cancer Center, all of whom contributed to a stimulating work environment and from all of whom I learned something either directly or by "osmosis" during this endeavour.

Table of Contents

List of Figures

List of Tables

List of Abbreviations and Symbols

BC	Backscatter Correction
EPID	Electronic Portal Imaging Device
FF	Flood Field
GLAaS	General Linear "calibration" Algorithm for amorphous Silicon
PSF	Point Spread Function
RHS	Right-Hand Side
ROI	Region of Interest
SF	Slit Field
TFT	Thin-Film Transistor
TM	Target Matrix
TPS	Treatment Planning System
D	Dose
f	Arbitrary Field
h_{ij}	Height at Position (i,j)
h_p	Radially-Dependent Function used in Kernel Expansion

k	Convolution Kernel
I_D	Discrete (pixel-by-pixel) Image
$I^R \equiv I_{raw}$	Raw EPID Image
i_0	Dark-Current EPID Image
I_{FF}	Flood-Field EPID Image
I^c	Corrected EPID Image
P	Pinnacle Response
Ψ	Energy Fluence
$\vec{r}$	Position Vector
r	Radius
R	Off-axis Response Function
s	Pixel Sensitivity Function

1 Introduction

Portal imaging is the most widely available method for evaluating and documenting the degree of geometric treatment accuracy in external beam therapy. Radiographic film has been used in the past for this purpose, and lately flat-panel Electronic Portal Imaging Devices (EPIDs) have been utilized to verify the geometric treatment accuracy in external beam radiation therapy. Dose verification is another application of portal imaging.

The approach is to calculate the portal dose image using a model, usually implemented in a Treatment Planning System (TPS), for comparison to that measured using a portal imager. If an EPID is to be used to determine the measured dose, and since the EPID response is likely to differ from that of water, there are two possible ways to compare measured and TPS dose maps. The first is to convert EPID readings to dose and the second is to directly simulate the EPID response. Both approaches have been reported in literature.

1.1 Active-Matrix EPIDs

Most flat-panel EPIDs currently in use are of the indirect detection active matrix type. They consist of a metal plate covered with a phosphor screen to generate light, plus an amorphous Silicon readout array. The readout array consists of light detecting photodiodes that are switched using thin film transistors (TFTs). Diodes detect light and readout is controlled by the transistor's gate. Each diode is first charged to a bias voltage

before being discharged by photons during irradiation. A diode is recharged when the transistor is open and the charge is measured. TFTs are activated one row at a time and all TFTs in a column are connected to one common external charge amplifier. The readout is thus performed one row at a time. The total array readout time is 0.04 - 0.5s. The diodes and TFT transistors in EPIDs need to be radiation resistant as they are exposed to the high doses in the radiation field. The switching and data acquisition electronics are located outside the field and they are not radiation resistant. EPIDs are usually 40cm x 30cm in size and have either a 512 x 384 pixel array or a 1024 x 768 pixel array. A diagram of a cross-section through an indirect-detection active matrix flat panel EPID is shown in Fig. 1-1 (Antonuk, 2002).

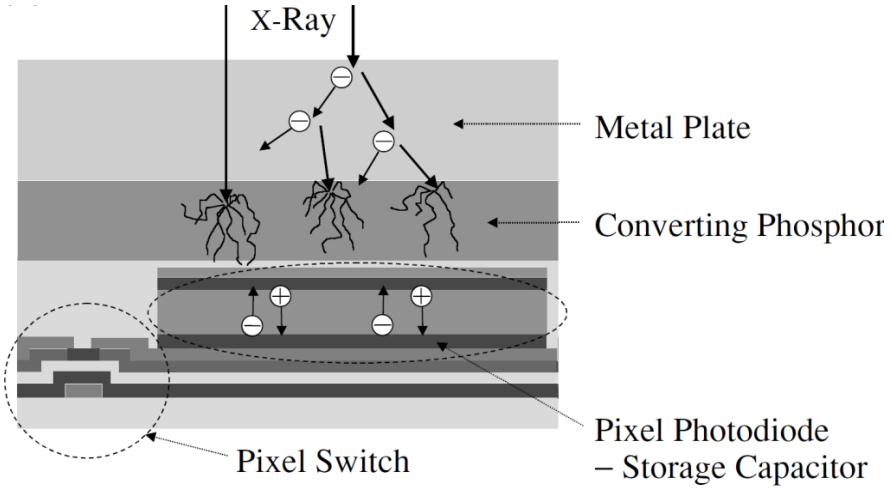

Figure 1-1: Cross-Section View of an Indirect-Detection Active Matrix Flat Panel EPID (Antonuk, 2002)

The characteristics for a Varian aSi EPID are shown in Table 1 (Antonuk, 2002).

Table 1-1: Technical Characteristics of Varian PortalVision aS500 EPID (Antonuk, 2002)

Detector Area	40.14 x 30.11 cm^2
Array Format	Monolithic Array
Pixel Format	512 x 384
Pixel Pitch	0.784 mm
Maximum Image Acquisition Rate	10 fps (frames averaged by hardware)
Image Display and Storage Time	2s per image
Digitization	14 bits
Metal Plate	1mm Cu
Scintillator	133 mg/cm^2 Gd_2O_2S:Tb

1.2 Linearity, Ghosting and Image Lag

Early work on EPID applications concentrated on determining if the dose response was linear and whether there was any dependence on the dose rate. It has been established by several authors (McCurdy, 2001; Grein, 2001; Greer, 2003; McDermott, 2004; Winkler, 2005, 2006) that the response of amorphous silicon EPIDs is linear in dose. It has also been shown that the response is almost independent of dose rate (Antonuk, 1998; El-Mohri, 199; McDermott, 2004). Early studies also evidenced two types of artifacts that can appear with EPIDs: ghosting and image lag (Siewerdsen, 1999; McDermott, 2004, 2006; Budgell, 2005). Such artifacts are due to the charge trapped within the photodiode layer resulting in both gain and offset effects. Ghosting is a gain effect whereby the trapped charge affects subsequent images. Image lag is an offset effect due to incomplete charge transfer from the pixel capacitor that is read-out in subsequent frames.

1.3 Energy Response

The EPID response at low energies is higher than that of water. This can be explained by the fact that the phosphor layer has a higher atomic number than water, as suggested by Greer (2009) and analyzed in detail by Partridge et al. (2010). The Compton mass attenuation coefficient is essentially independent of the atomic number, whereas the mass Photoelectric attenuation coefficient is proportional to the cube of the atomic number (Podgorsak, 2005). As a consequence, at photon energies below 500keV, where the photoelectric effect becomes important (Partridge et al., 2010), the mass attenuation coefficient of a high atomic number material begins to increase compared to that of water. Consequently, the high-atomic-number phosphor, has a higher low-energy response than water. In practice, the difference in energy response between the dose in water and the EPID manifests itself as an increased EPID response away from the beam axis due to the off-axis beam softening induced by the flattening filter. This effect needs to be accounted for when performing dose verification.

1.4 Sensitivity Calibration

Individual photodiodes and amplifiers in EPIDs are not identical. To correct for the variations in individual photodiodes, a dark field and flood field image are acquired. To avoid the influence of noise, several images are acquired and then averaged for both flood field and dark-field images. The actual EPID image is then processed pixel by

pixel by subtracting the dark-field image, i_0, and then normalizing (dividing) the result by the flood field image to obtain the corrected image:

$$I^c = \frac{I^R - i_0}{I_{FF}} \tag{1.1}$$

Theoretically, the dark-field image should also be subtracted from the flood-field image in the denominator but, because the dark-field image values are much smaller than the flood-field image values, Eq. (1.1) is considered adequate. Dark-field and flood-field corrections are performed automatically by the image acquisition software. Aside from eliminating pixel-to-pixel sensitivity variation, the division by the flood field also inadvertently removes any features of the beam, such as "horns" induced by the flattening filter. In order to perform a fair comparison between simulated and measured dose, these features have to either be artificially restored in the EPID image or a division by the flood field has to be performed for the simulated dose.

1.5 Spatial Resolution: Scatter and Glare

EPID spatial resolution depends mostly on scatter in the metal plate and light spread in the phosphor screen. Light spread in the phosphor is referred to as "glare" although some authors reserve that term for a situation encountered in older, TV-camera-based, EPIDs whereby photons emitted at large angles to the normal get reflected by the mirror and phosphor screen and then enter the camera lens as if emitted from a different point on the phosphor screen. Scatter and glare need to be accounted for when performing dose verification.

1.6 Support-Arm Backscatter

EPIDs are held in place by a support arm, which is located underneath the flat panel. Also underneath the flat panel are located a pair of steel bars and wires. Figure 1-2 (Ko, 2004) depicts the support arm and other structures located underneath the flat-panel EPID. Radiation backscattered from these structures into the EPID introduces artificial asymmetries in the EPID image. The effect is known as "non-uniform backscatter" and has to be accounted for when performing dose verification.

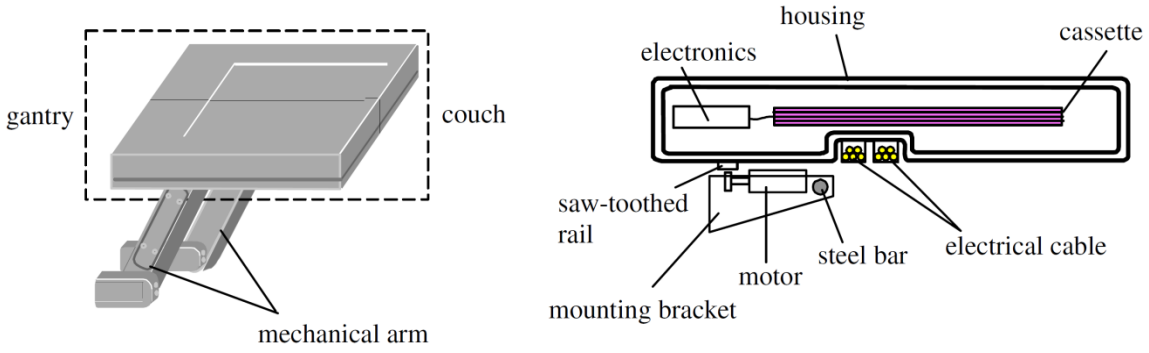

Figure 1-2: Structures Located Underneath The Flat Panel (Ko, 2004)

Because of the convenience of using EPIDs, the past decade has seen significant work dedicated to developing methods for overcoming their shortcomings when used as dosimeters and this is still an active area of investigation. The subsequent chapter reviews the methods developed so far for overcoming the three main weaknesses of EPIDs when used as dosimeters: scatter and glare, increased response at low energies and non-uniform backscatter.

2 Review of Progress to Date in Pre-Treatment Dose Verification Using aSi EPIDs

As mentioned in the introduction, there are three main challenges in using aSi EPIDs as dosimeters:

1. Scatter and glare
2. Increased response at low energy resulting in increased response away from the axis
3. Non-uniform response due to non-uniform backscatter.

This chapter will review approaches to date in dealing with these challenges either individually, or in some combination.

2.1 Scatter and Glare

To account for scatter and glare, the EPID image is usually expressed as a convolution between the primary fluence and a position invariant kernel. Different approaches of determining the kernel have been reported.

Van Esch (2004) studied EPID characteristics including linearity with dose and dose rate, as well as comparisons between TPS-generated dose maps and EPID images. To account for scatter and glare, a translation-invariant "dose deposition kernel" was used, in the form of three Gaussians. The parameters of the dose deposition kernels were determined by fitting computed images to acquired images.

Warkentin (2003) constructed the kernel as a convolution of a "dose deposition kernel" (determined via Monte Carlo calculations using EGS-NRC (Kawrakow, 2002) to account for scatter of high-energy photons) and an optical glare kernel determined empirically. For verification purposes, instead of comparing the EPID image with the kernel-blurred TPS image, the authors recommended de-convolving the composite kernel out of the EPID image by using a fast Fourier transform. The primary fluence was subsequently convolved with a "water-phantom kernel" calculated using EGS-NRC and the resulting dose at 10 cm water depth was compared with that calculated by the TPS. The method was subsequently extended (Steciw, 2005) to predict the dose in an anthropomorphic phantom. To achieve that, the ratio between the primary fluence profile for a given MLC-defined beam and the primary fluence profile for a corresponding open field was used to define an artificial MLC attenuation in the TPS. The TPS was then used to calculate the 3D dose in the anthropomorphic phantom.

Kirkby (2005) reported a similar kernel-convolution method but used Monte Carlo calculations to model both scatter and optical glare. Additionally, in the same work, the calculated combined scatter and glare kernel was fitted using a triple exponential.

$$k(r) = e^{-P_1 r} + P_2 e^{-P_3 r} + P_4 e^{-P_5 r} \tag{2.1}$$

2.2 Increased Off-Axis Response

Translation-invariant kernels are not enough to model the full EPID response. The increased off-axis response also needs to be taken into account. To do so,

Greer (2005) proposed an approach that starts by expressing the raw image as the product between the azimuthally-symmetric energy fluence, Ψ, off-axis response, R,and pixel sensitivity, *s*:

$$I^R(x,y) = \Psi\left(\sqrt{x^2+y^2}\right) R\left(\sqrt{x^2+y^2}\right) s(x,y) \tag{2.2}$$

By sliding the EPID in the cross-plane direction, and recording the signal on the axis, the cross-plane pixel sensitivity profile $s(x,0)$ is obtained. By dividing the flood-field cross-plane profile by the cross-plane pixel-sensitivity profile, the product between the energy fluence and off-axis response is obtained:

$$\Psi(x)R(x) = \frac{I^R(x,0)}{s(x,0)} \tag{2.3}$$

The radial dependence of the fluence is determined by ion-chamber measurements and is subsequently divided out of the product, allowing the calculation of the off-axis response, $R(x)$.

Another approach for addressing the increased off-axis response was proposed by Li (2006). He proposed to replace Warkentin's (2003) convolution method with a superposition method whereby the energy response kernel is radially dependent. The radial dependence is approximated by dividing the distance between the interaction point and the beam axis into five regions and using a different convolution kernel for each region.

$$D(r) = \sum_i \int_{R_i} \Psi_i(\vec{r}\,') k_i \left(\left| \vec{r} - \vec{r}\,' \right| \right) d^2 \vec{r}\,' \tag{2.4}$$

Each of the five kernels are calculated using a Monte-Carlo code developed in house, based on EGS4. The fluence is determined indirectly from the TERMA exported from the TPS (Pinnacle) and additional corrections are applied to account for MLC transmission.

Greer has subsequently proposed a method (Greer, 2009) whereby the translation-invariant triple-exponential kernel in Eq. (2.1) developed by Kirkby (2005) was used in conjunction with radially-dependent fluence attenuation factors (Greer, 2007) to account for both scatter/glare and off-axis response. Greer (2009) also accounts for non-uniform backscatter by replacing the flood-field correction with a "Pixel Sensitivity Matrix" (PSM) correction. The PSM is obtained by removing the backscatter component from the flood field. The backscatter component is, in turn, calculated as the ratio between the on-arm and off-arm flood field EPID image. It is worth mentioning that, even after the PSF correction, test-field images are still influenced by the field-dependent backscatter.

Parent (2006) studied the effect of off-axis softening by Monte Carlo simulation of offset fields using the BEAM-NRC code and compared results with EPID-measured values. To avoid dividing out the flattening-filter "horns", EPID calibration was performed using a modified form of Eq. (1.1), in which the flood-field is replaced by a composite "gain image" created by setting the collimator to deliver a 10cm x 10 cm field and sliding the

EPID so that different areas are irradiated successively. The corrected image was calculated as:

$$I^c = \frac{I^R - i_0}{I^{gain} - i_0} \tag{2.5}$$

Because I^{gain} does not contain the "horns", the correction applied by Eq. (2.5) does not artificially remove them. The authors found very good agreement between Monte Carlo results and measurements (output factors and profiles). It is to be mentioned that the images were acquired using an Elekta EPID whose support arm is located to one side and is not irradiated by the beam. Consequently, backscatter is uniform.

The off-axis EPID response can also be modelled using the TPS by adjusting machine parameters in the TPS model such that the calculated dose map matches as closely as possible the EPID response. This approach was followed by Khan et al. (Khan, 2008). A dedicated machine model was created within a Pinnacle^3 (Philips Medical Systems, Madison, Wi) version 7.4f TPS. The model parameters were tuned so that calculated planar dose maps of a set of rectangular fields delivered to a water phantom at 3 cm depth and 100 cm SSD matched the corresponding set of acquired Varian aS500 EPID images. The adjustable parameters were: photon energy, primary fluence profile, primary source size, secondary source width and strength, jaw and multi-leaf collimator (MLC) transmission, and MLC rounded leaf tip radius.

A practical method to reduce the effects of off-axis softening is to introduce a Cu plate underneath the top EPID cover. Such a plate attenuates the low-energy photons, to which

the EPID over-responds. This method was investigated, among others, by Yeboah (2000) and Talamonti (2006).

An original method for converting EPID images to a dose map without making use of scatter and glare kernels was proposed by Nicolini (2006) under the name of General Linear "calibration" Algorithm for amorphous Silicon (GLAaS). The method relies on expressing the EPID dose response curve using a linear relationship between the corrected EPID image and dose:

$$D = mI^c + q \tag{2.6}$$

The dose is measured using an ion-chamber or diamond detector. Parameters m and q are determined for several rectangular and square fields at different depths as well as for radiation transmitted through the MLC. For each depth, the m and q parameters are expressed as a function of the effective square field size, l, determined using the usual perimeter-to-area equivalence relationship. For an IMRT field comprised of several segments, each characterized by weight w_s, the formula for calculating the dose based on the EPID image becomes:

$$D(\vec{r}) = \sum_s \left[m^{open}(l_s) w_s(\vec{r}) I(\vec{r}) + q_s^{open} \right] + m^{trans} \left(1 - \sum_s w_s(\vec{r}) \right) I(\vec{r}) + q^{trans} \tag{2.7}$$

In the above equation, the position-dependent weight is taken to be equal to the weight for the respective segment for points in the open region of the field and zero for points blocked by the MLC.

In its initial form, the GLAaS algorithm did not account for the radial dependence of the dose or for the non-uniform backscatter because it relied on the flood-field corrected EPID image. In a later version, (Nicolini, 2008), the algorithm was enhanced to account for these two effects. In the new version, the radial dependence of the dose is reconstructed by first calculating a correction matrix by taking the ratio of the TPS-calculated dose to the plain GLAaS reconstructed dose at a given depth and SSD for a flood field. The correction matrix is then used to multiply the "open" component of the dose.

To account for the non-uniform support-arm backscatter, a simple correction, depending linearly on the in-plane position of the point, is applied to the "open" component of the dose. The slope of the linear correction is determined experimentally for different square fields.

Originally applied to IMRT, the GLAaS algorithm was also shown to work for RapidArc applications (Nicolini, 2008).

2.3 Non-Uniform Backscatter

The effects of non-uniform backscatter induced by the support arm and the ways to account for them have been studied by many authors. For example, Ko (2004) has shown that the non-uniformity introduced by support-arm backscatter is approximately 5% of the central axis signal. To reduce the non-uniformity, Ko studied the addition of a Cu or Pb metal plate downstream from the phosphor. The plate provides increased, uniform,

backscatter to the phosphor and also attenuates the non-uniform backscatter from the support arm. In general, the addition of material downstream from the phosphor leads to an increase in signal because of backscatter. However, because of the finite range of electrons, the increase saturates beyond a certain material thickness. Ko (2004) determined the saturation thickness using Monte Carlo calculations and then used plates of the calculated thickness. The saturation thickness for Pb was found to be 3mm for 6MV beams and 6.8 mm for 18MV beams. The corresponding values for Cu were 20.6 and 22.6 mm. 50 mm of water were found to be insufficient to provide saturation for either 6MV and 18MV beams. The authors' final recommendation was to use a 5-mm lead plate. Their computational results were verified against actual measurements in a subsequent paper (Moore, 2005).

A different approach to arm backscatter was taken by Siebers et al. (2004). In their approach, no allowance was made for scatter or glare. To convert the EPID image into dose, first, a Monte Carlo model of the imager was prepared, using detailed geometric information. The support arm and other structures underneath the imager responsible for backscatter were represented by a uniform slab of water located underneath the imager model. The thickness of the backscatter water slab was determined such that the ratio of the EPID average reading for a 10cm x 10cm to that of a flood field was equal to the same ratio calculated using the Monte Carlo model:

$$\frac{\bar{I}_{10X10}^{EPID}}{\bar{I}_{FF}^{EPID}} = \frac{\bar{D}_{10X10}^{MC}}{\bar{D}_{FF}^{MC}} \tag{2.8}$$

Once the MC model was finalized with the addition of the uniform backscatter material, a "calibration correction matrix", C, was determined by taking the ratio between the (corrected) EPID image and the MC dose for a flood field at 20cm depth of water, which corresponds to a situation where the dose is almost flat. In that case, the correction matrix accounts both for pixel-to-pixel sensitivity variation and for the flattening-filter-induced "horns".

$$C(\vec{r}) = \frac{I^c(\vec{r})}{D^{MC-20cm}(\vec{r})} = \frac{\frac{I_{raw}^{20cm-FF}(\vec{r})}{I_{raw}^{0cm-FF}(\vec{r})}}{D_{FF}^{MC-20cm}(\vec{r})} \cong \frac{1}{I_{raw}^{0cm-FF}(\vec{r})} \tag{2.9}$$

Multiplying the correction matrix by the MC result for an arbitrary field is equivalent to applying the flood-field correction and hence allows direct comparisons to the (corrected) EPID image.

In 2010, Berry et al. (Berry, 2010) proposed a simple way to account for non-uniform backscatter by simply correcting for the in-plane asymmetry. For a given square field size, d, the backscatter correction matrix is defined as the ratio of two corrected images:

$$BC_d(x,y) = \frac{I_d^c\left(x,|y|\right)}{I_d^c(x,y)} \tag{2.10}$$

In Eq. (2.10), the y coordinate varies along the in-plane direction, is zero on the central axis and increases towards the gantry. For an arbitrary field f, inscribed in a square of size d, the comparison is made between the backscatter-corrected EPID image:

$$I_{BC}(\vec{r}) = I_f^c(\vec{r}) BC_d(\vec{r}) \tag{2.11}$$

and the TPS-calculated dose map, D_{TPS}.

The authors also proposed a simplified backscatter correction, which depends only on the in-plane coordinate, y, through a linear relationship:

$$BC_d(x,y) \cong \begin{cases} 1 & y > 0 \\ 1 + m_d y & y < 0 \end{cases} \tag{2.12}$$

The dependence of the slope, m, on the field size is fitted using a fourth-order polynomial.

Cufflin et al. (Cufflin, 2010) were successful in simulating the EPID response using a detailed Monte Carlo model of the EPID. Non-uniform backscatter was simulated by adding blocks of water of different thicknesses underneath the EPID. The authors mention that the thickness and position of the water blocks was adjusted iteratively but no mention is made regarding whether the adjustment followed a systematic algorithm or was performed by trial and error.

To model the non-uniform support-arm backscatter, Rowshanfarzad et al. (Rowshanfarzad, 2010) improved on Greer's (2009) model by adding a "backscatter" kernel. Since convolution with a translation-invariant kernel can only model uniform backscatter, to model the non-uniformity, the authors only applied the convolution over the region that projects onto the support arm. The scatter and glare kernel, as well as backscatter kernel, were convolved with the TERMA extracted from the TPS. The backscatter kernel was determined both by measurement, using 1-cm^2 "pencil" beams

and by MC simulation using EGS-NRC/BEAM. Subsequently, Rowshanfarzad (2010) proposed to reduce the effect of non-uniform arm backscatter in a manner similar to that presented by Ko (2004) by adding a Pb plate between the EPID cassette and the support arm. After studying different thickness values and weighing the benefit of backscatter reduction versus added weight of the EPID, the authors recommended a 2-mm thickness, smaller than the 5-mm thickness recommended by Ko (2004). They commented that the additional reduction in non-uniformity introduced by increasing the thickness to 5mm does not justify the additional weight.

3 Modelling the Effect of Non-Uniform Backscatter from the Support Arm

The modeling of the EPID response, including non-uniform backscatter, can be accomplished either by using commercial treatment planning systems, or by using alternative methods such as Monte Carlo simulation or convolution kernels. The majority of methods proposed so far for addressing the non-uniform backscatter effect rely on tools or measurements outside of the common clinical setting, such as MC codes or measurements performed with the EPID removed from the support arm. This chapter presents a method for addressing the non-uniform backscatter that can be easily implemented in clinical practice using a common TPS and that does not require the modification of the EPID or its removal from the support arm.

3.1 General Approach

To ensure a fair comparison between the TPS-calculated planar dose and the EPID response, the TPS model needs to be able to calculate the EPID dose for any given field, including "horns" due to the flattening filter and the effect of non-uniform support-arm backscatter. Because the automatic flood-field correction applied to the EPID image removes features such as "horns" and the effect of flood-field non-uniform backscatter, these features need to first be restored to the corrected EPID image before the comparison can be made. If an adequate TPS model of the EPID is available, the features can be

restored into the corrected EPID image by simply multiplying that image by the TPS-calculated planar dose for a flood field, as demonstrated below.

The raw EPID image $I^R(f)$ for an arbitrary field f depends on the EPID dose for field f, D(f), the dark current i_0 and the pixel sensitivity s:

$$I^R(f)=s\cdot D(f)+ i_0 \tag{3.1}$$

To eliminate the pixel-to-pixel sensitivity variation, the image acquisition software automatically calculates the corrected EPID image, $I^c(f)$, by subtracting the dark current and dividing by the (raw) flood-field (FF) image, $I^R(FF)$:

$$I^c(f)=[I^R(f)- i_0]/I^R(FF) \tag{3.2}$$

It follows that the corrected EPID image equals simply the ratio of field-of-interest to flood-field EPID doses.

$$Ic(f)=[IR(f)- i0]/IR(FF)=[s\cdot D(f)]/[s\cdot D(FF)]= D(f)/D(FF) \tag{3.3}$$

For any arbitrary field f, a "corrected" TPS dose can be defined, by analogy with eq. (3.3), as the ratio of the TPS-calculated dose for the field of interest to the TPS-calculated dose for the flood field:

$$P^c(f)= P(f)/P(FF) \tag{3.4}$$

In eq. (3.4), P(f) denotes the TPS (Pinnacle^3) planar dose for the field f. If an accurate model of the EPID is implemented in the TPS, it is reasonable to expect the "corrected" TPS-calculated dose to be equal to the corrected EPID image, that is:

$$P^c(f) = P(f)/P(FF) = D(f)/D(FF) = I^c(f) \quad (3.5)$$

Multiplying eq. (3.5) by the TPS-calculated dose for a flood field, P(FF), it is easy to see that the TPS-calculated dose P(f) is equal to the product between the corrected EPID image and the TPS-calculated planar dose for a flood field:

$$P(f) = I^c(f) \cdot P(FF) \quad (3.6)$$

The role of the multiplication by P(FF) is to restore the features removed by the automatic flood-field correction. Consequently, the RHS of eq. (3.6), will be called the feature-restored EPID image. It represents, for any practical purpose, the EPID dose, D(f). Equation (3.6) can constitute the basis for QA verification of the field, based on comparing the TPS-calculated planar dose, P(f), with the feature-restored EPID image.

The validity of eq. (3.6) depends on the accuracy of the EPID model in the TPS. The challenge in modelling the EPID comes primarily from the presence of non-uniform backscatter due to the support-arm and, to a lesser extent, from the different energy response of the EPID and TPS. The exact position and composition of the arm, cross-bars and cables is difficult to assess and model. To avoid the need for exact knowledge about the position and composition of the materials in the support-arm, a novel approach is used, as described below.

A composite slit-field (SF) is constructed by superposing the dose from a sequence of 32 individual slit-field irradiations, sf_i, as detailed in section 3.2. Backscatter effects can be assumed to be negligible for such a slit field. When applied to a composite slit field, eq. (3.6) is re-written (by replacing f with SF):

$$P(SF) = I^c(SF) \cdot P(FF) \tag{3.7}$$

Because the slit-field dose does not include backscatter, the only feature of the corresponding (EPID as well as TPS) dose map is the "horns" induced by the flattening filter. In the case of the EPID, division by the flood field image removes "horns" and, additionally, divides out the effect of flood-field non-uniform backscatter. As a consequence, the corrected composite slit field image, $I^c(SF)$, represents, for any practical purpose, the inverse (reciprocal) of the flood-field non-uniform backscatter effect. By rearranging eq. (3.7), it can be shown that the TPS-calculated flood-field dose must equal the ratio between the TPS-calculated dose for the composite slit-field and the corrected EPID image for the same:

$$P(FF) = P(SF)/I^c(SF) \tag{3.8}$$

We refer to the right hand side of eq. (8) as a "target matrix", $TM=P(SF)/I^c(SF)$. Noting from before that the composite slit-field contains only "horns" and that the corrected composite slit-field image is the reciprocal of the non-uniform backscatter effect, it follows that the TM includes both. The TM represents the flood-field EPID dose, D(FF), or, equivalently, the (raw) EPID response if pixel sensitivity was the same for all pixels. It can also be interpreted as the corrected EPID image that would be obtained if the flood field used for calibration was uniform, without "horns" or non-uniform backscatter effects. Due to the negligible backscatter effects, there is no need to model the support-arm in the TPS when calculating the SF dose, P(SF). This allows the TM to be calculated before an appropriately-shaped support-arm region is available for the TPS model. The

backscatter ROI representing the support arm is added to the TPS model only after calculating the TM and adjusted iteratively until the TPS-calculated flood-field dose becomes equal to the TM (hence the name "target matrix"). Once the appropriate backscatter ROI is found, eq. (3.6) can be assumed to be satisfied for any field f and can be used to set up a QA procedure consisting of four steps:

[1] Acquisition of a (corrected) EPID image for the field to be verified

[2] Multiplication of the EPID corrected image by the TPS flood-field dose to determine the feature-restored EPID image.

[3] TPS calculation of the planar dose (using a model that includes a backscatter ROI)

[4] Comparison of the TPS planar dose with the feature-restored EPID image. If the two match within established criteria, the field passes QA inspection.

3.2 Construction of the Composite Slit Fields

Composite slit fields are constructed using a method previously developed at the Juravisnki Cancer Center. Individual slit-fields, sf_i, are constructed using MLC collimated slits oriented both in-plane and cross-plane. In either case, all leaves on the same bank are aligned and expose a 0.5 cm gap to the leaves on the opposite side. In-plane slit-fields measure 0.5 cm in width (cross-plane direction) by 30 cm in length (in-plane direction) so that each spans the full 30 cm in-plane length of the EPID. Asymmetric jaws are fixed at X1 = 0.5 cm and X2 = 15 cm while the gap formed by

opposing MLC leaf banks is successively offset in the cross-plane direction from 0 to 15 cm in 1 cm increments. The MLC and jaw settings are then mirrored and the sequence is repeated so that the in-plane slit-fields span the other half of the EPID. The combined 32 individual in-plane slit-fields therefore span the central 30 cm of the EPID. With the collimator set to 90 degrees, cross-plane slit-fields measuring 40 cm in width by 0.5 cm in length successively irradiate the half of the EPID closest to the gantry. The collimator is then set to 270 degrees (i.e., rotated 180 degrees from its previous position) to successively expose the other half of the EPID (the half farthest from the gantry) with the same sequence. The combined 32 cross-plane slit-fields therefore span the entire EPID area. Each slit is programmed to deliver 50 MU and dose is scored separately for each slit-field in the sequence.

For the Pinnacle^3 slit-field model, a uniform, unit density backscatter slab, 0.5 cm thick and adjacent to the exit surface of the build-up region is used to represent the EPID. The composite dose-plane image is then constructed by applying a threshold level (all values below the threshold are set to zero) to each individual slit-field dose-plane image before summing the doses. The threshold level is selected so that each voxel in the composite dose-plane image receives a non-zero dose from a single slit-field dose-plane image.

For the EPID slit-field, an EPID image of each individual Pinnacle^3 slit-field is acquired. Each image is inverted by subtracting the value of each pixel from the theoretical maximum so that higher pixel intensity corresponds to higher dose. A composite image is constructed by applying a threshold to each slit-field image and summing as described

above. Both Pinnacle^3 and EPID composite slit-field images appear as a series of bright lines separated by dark (null) pixels that correspond to regions in the individual slit-field images with pixel values below the threshold. The dark pixels are re-assigned a value determined from the brightest pixels on either side of the dark region in order to obtain a somewhat smoothed image. The smoothed in-plane and cross-plane composite slit-field images are then averaged together.

3.3 No-Backscatter TPS Model

A Pinnacle^3 machine model is developed with parameters adjusted to best fit profiles and output factors derived from a representative set of EPID images. A realistic energy spectrum is used. The off-axis softening is substantially increased and other model parameters are adjusted so that calculated profiles fit those measured by Ko, Kim and Siebers (2004).

3.4 Construction of the Target Matrix

The target matrix is calculated by taking the ratio of Pinnacle^3 to EPID averaged composite slit-field images. The ratio image is smoothed using a Gaussian blur filter with a sigma of 20 pixels. The target matrix is then re-normalized with respect to its central pixel value. The processing of the slit-field dose-planes and images into composite slit-field dose-planes and images and the construction of the target matrix is automated through the use of scripts based on ImageJ. The target matrix corresponds to the right

hand side of eq. (3.8). This image approximates the image of a flood-field that the EPID would record if the calibration flood field image was obtained under uniform field and uniform backscatter conditions. In contrast to other approaches, this image is determined without removing the EPID from the support-arm.

3.5 Construction of the Backscatter ROI

To account for the non-uniform backscatter in the TPS calculation, a variable-thickness backscatter ROI is introduced. This ROI is defined by its thickness $h_{i,j}$ at fixed grid points (x_i, y_j) located on a 9 x 13 grid and assuming linear variation of the thickness between the points. The 9x13=117 variables $h_{i,j}$ defining the height at the grid points are treated as optimization parameters that are varied in order to minimize the difference between the LHS and RHS of eq. (3.7) at the grid points, in a least-squares sense. In particular, both the TPS flood-field planar dose, P(FF), and the target matrix, TM=P(SF)/I^c(SF), are first approximated as linear combinations of bivariate Lagrange Polynomials (Epperson, 2002)

$$F_{i,j}(\vec{r}) = \left(1 - \frac{x - x_i}{a}\right)\left(1 - \frac{y - y_j}{b}\right); \quad -a < x < a; -b < y < b \tag{3.9}$$

In eq. (3.9), a and b correspond to the distance between grid points in the *x*- and *y*-directions respectively. The TPS response is therefore approximated as:

$$P_{FF}(\vec{r}, h_{0,0}, \ldots h_{8,12}) \cong \sum_{\substack{i=0,8 \\ j=0,12}} {}^{TPS}c_{i,j} F_{i,j}(\vec{r}) \tag{3.10}$$

and the target matrix is approximated as:

$$TM(\vec{r}) \cong \sum_{\substack{i=0,8 \\ j=0,12}} {}^{TM}c_{i,j} F_{i,j}(\vec{r}) \tag{3.11}$$

A graphical depiction of the *TM* representation is shown in Fig. 3-1. Similar representations are used for the ROI and P_{FF}.

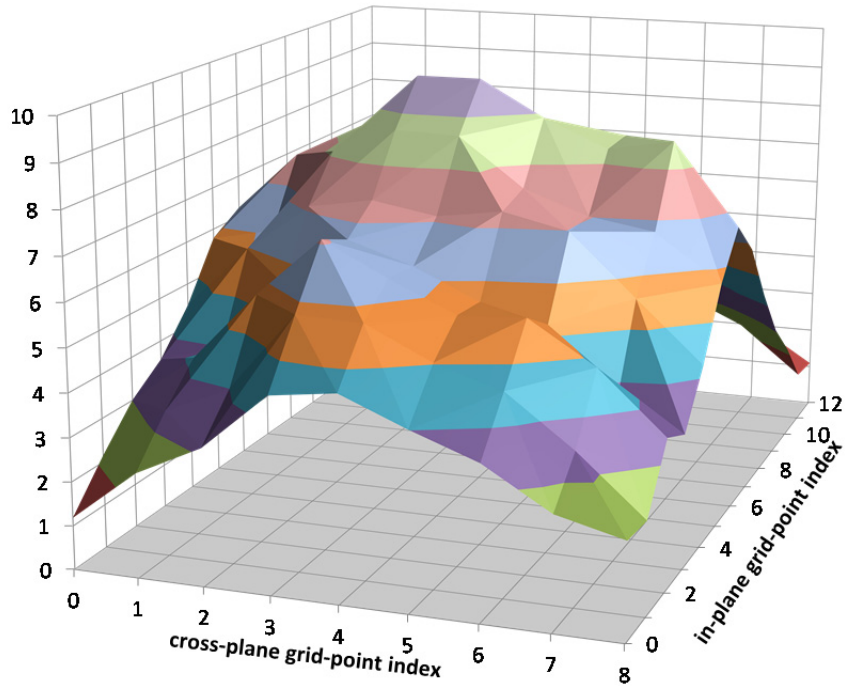

Figure 3-1: Approximate Representation of the *TM*. The height at each grid point represents ${}^{TM}c_{ij}$.

Expansion coefficients ${}^{TPS}c_{ij}$ are found by minimizing the error between the linear-combination representation and the actual TPS response in a least squares sense, that is by minimizing:

$$\int \left[P_{FF}(\vec{r}, h_{1,1}, \ldots h_{9,12}) - \sum_{\substack{i=0,8 \\ j=0,12}} {}^{TPS}c_{i,j} F_{i,j}(\vec{r}) \right]^2 d^2\vec{r} \tag{3.12}$$

Similarly, expansion coefficients ${}^{TM}c_{i,j}$ are found by minimizing the error between the linear-combination representation and the actual target matrix in a least squares sense, that is by minimizing:

$$\int \left[TM(\vec{r}) - \sum_{\substack{i=0,8 \\ j=0,12}} {}^{TM}c_{i,j} F_{i,j}(\vec{r}) \right]^2 d^2\vec{r} \tag{3.13}$$

The respective systems of equations are found by taking the derivative with respect to each coefficient and making it equal to zero. For the TPS response, the linear system is written as:

$$\int \left[P_{FF}(\vec{r}, h_{1,1}, \ldots h_{9,12}) - \sum_{\substack{i=0,8 \\ j=0,12}} {}^{TPS}c_{i,j} F_{i,j}(\vec{r}) \right] F_{k,l}(\vec{r}) d^2\vec{r} = 0 \tag{3.14}$$

which is equivalent to:

$$\sum_{\substack{i=0,8 \\ j=0,12}} {}^{TPS}c_{i,j} \int F_{i,j}(\vec{r}) F_{k,l}(\vec{r}) d^2\vec{r} = \int P_{FF}(\vec{r}, h_1, \ldots h_{108}) F_{k,l}(\vec{r}) d^2\vec{r} \tag{3.15}$$

This equation determines the set of coefficients ${}^{TPS}c_{i,j}$ used to represent the computed planar dose, P_{FF} (via eq. 3.10), for a given backscatter ROI specified by its heights $h_{i,j}$ at each grid point (i,j).

Similarly, for the target matrix, the linear system is written as:

$$\sum_{\substack{i=0,8 \\ j=0,12}} {}^{TM}c_{i,j} \int F_{i,j}(\vec{r}) F_{k,l}(\vec{r}) d^2\vec{r} = \int TM(\vec{r}) F_{k,l}(\vec{r}) d^2\vec{r} \tag{3.16}$$

This equation determines the set of coefficients ${}^{TM}c_{i,j}$ used to represent the target matrix TM via eq. (3.11). Since the goal is to determine the backscatter region, which is specified by the set of heights, $h_{i,j}$, these heights are subsequently adjusted iteratively until:

$${}^{TPS}c_{i,j}(h_{0,0},...h_{9,13}) = {}^{TM}c_{i,j} \tag{3.17}$$

that is until the calculated planar dose matches the target matrix.

At each iteration step, the ROI thickness at point (i,j) is updated using:

$$h_{i,j}^{m+1} = h_{i,j}^{m} \frac{{}^{TM}c_{i,j}}{{}^{TPS}c_{i,j}^{m}} \tag{3.18}$$

When convergence is achieved, the following holds true:

$$h_{i,j}^{conv} = h_{i,j}^{conv} \frac{{}^{TM}c_{i,j}}{{}^{TPS}c_{i,j}^{conv}} \Leftrightarrow {}^{TPS}c_{i,j}^{conv} = {}^{TM}c_{i,j} \tag{3.19}$$

Once the heights of the backscatter ROI are determined, the ROI is added to the Pinnacle^3 model in a manner consistent with the dataset, by defining a series of axial contours, one for each dataset voxel plane, using the Pinnacle^3 scripting language. A sample ROI axial contour, is shown in fig. 3-2.

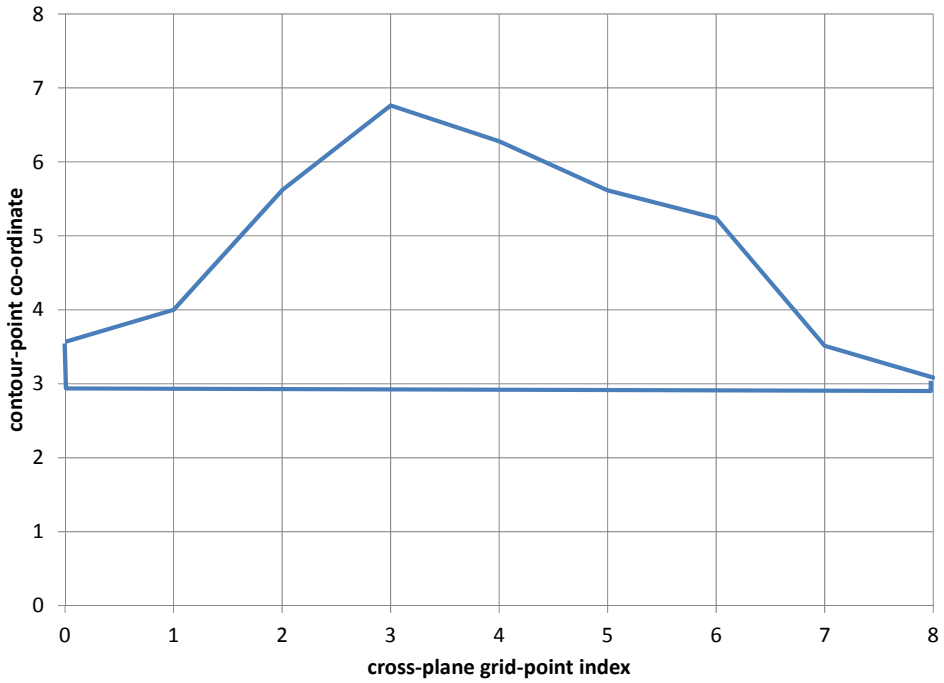

Figure 3-2: Sample ROI Axial Contour

The Pinnacle[3] script to set up all the ROI contours is generated automatically based on the ROI heights, using a PERL script.

3.6 Results

3.6.1 Slit Fields

Slit-field planar dose calculations in Pinnacle[3] were based on a uniform backscatter region. These calculations were repeated with a full phantom backscatter region as well as with the optimized variable thickness backscatter region, but no significant differences in normalized slit-beam profiles were observed. This confirms the assumption that backscatter effects are negligible for slit beams and, consequently, for the composite slit field.

In-plane and cross-plane composite EPID slit-fields are illustrated in Fig. 3-3 (a) and (b) respectively. Plots of selected individual slit-field profiles are shown in Fig. 3-3(c) and (d) below their respective composite slit-fields.

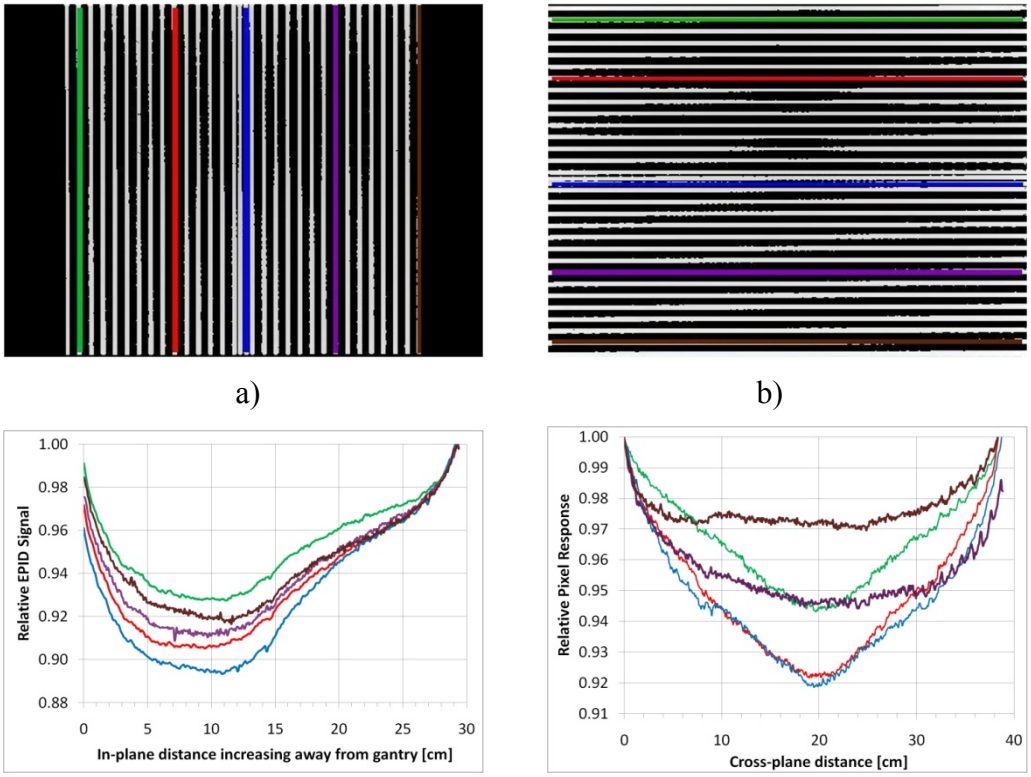

Figure 3-3: Composite in-plane (a) and cross-plane (b) slit-field images formed by composing a series of 32 individual slit-field EPID images.

A threshold is applied to each individual slit-field image to null all but a narrow strip. Each strip in the composite slit-field image corresponds to a single individual slit-field image. The colored lines in (a) and (b) correspond to the slit beam profile curves plotted in (c) and (d) respectively.

As explained in section 3.1, the corrected slit field image, $I^c(SF)$, can be interpreted as the inverse (reciprocal) of the arm backscatter effect and hence it dips in regions with high backscatter. In-plane profiles of EPID slit-field (corrected) images plotted in Fig. 3-3 (c) indicate that the effect of backscatter is greatest along the centre, while cross-plane

profiles plotted in Fig 3-3 (d) are most affected towards the gantry. The shape is consistent with the support arm and associated electronics, which are responsible for most of the non-uniform backscatter. There is greater than 9% variation in signal due to the absence of backscatter. Both sets of plots are consistent with fig. 2 (c) in Ref. 3 (which depicts the effect of support-arm backscatter), further supporting the assumption that backscatter is negligible for slit beams.

3.6.2 Pinnacle^3 model of the EPID in the no-backscatter geometry

The Pinnacle3 EPID machine model is designed to reproduce the EPID response in the no-backscatter geometry as measured by Ko, Kim and Siebers (2004). Table 1 shows the values used for the TPS model parameters.

Table 3-1: Pinnacle^3 machine parameters used for modeling EPID response

Parameter	***Value***
Energy spectrum	Tuned to match depth dose in water
Electron Contamination	Turned off
Spectral Off-Axis Softening Factor	18
Radial fluence profile	Adjusted from clinical beam data to fit profiles measured by Ko, Kim, and Siebers
Effective Source Size	0.04 cm in both x and y directions
Flattening Filter Scatter Source	Gaussian Height = 0.1; Gaussian Width = 1.3
Top/Bottom Jaw Transmission	0.007
Left/Right Jaw Transmission	0.007
MLC Transmission	0.015
Rounded Leaf Tip Radius	6 cm
Tongue and Groove width	0.1 cm
Additional interleaf leakage transmission	0.02

Measured and calculated EPID response profiles for various square field sizes are compared in fig. 3-4. The slight error in calculated profile width may be attributed to error in digitizing from the small scale of fig. 2 of Ko et al. (2004). Since their measurements were made with the imager at 105 cm SDD, the field dimensions in the current Pinnacle[3] model are scaled in order to match the profile width at 100 cm SDD.

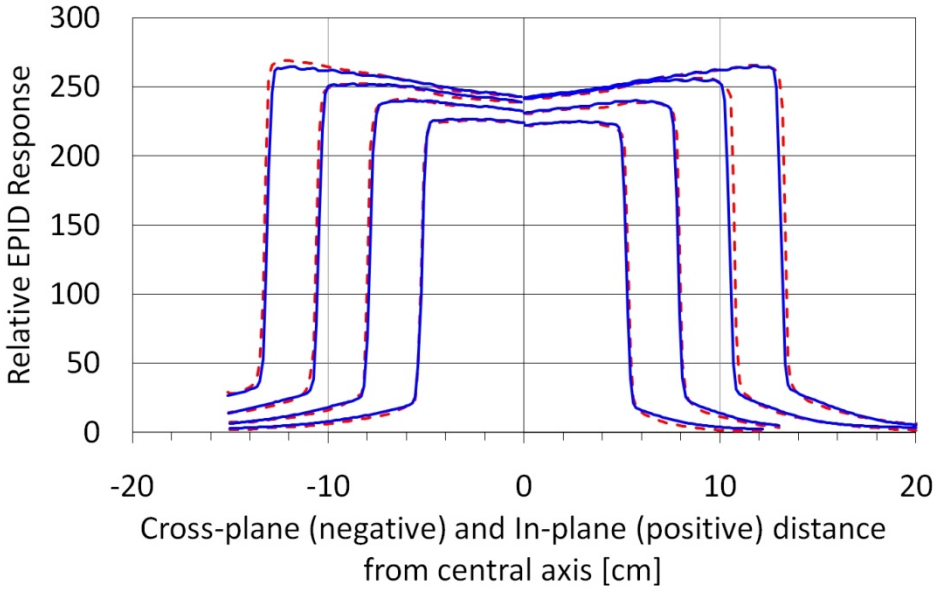

Figure 3-4: Pinnacle[3] calculated EPID response profiles (solid lines) compared to those published by Ko et al., which were measured in the no-backscatter geometry (dashed lines).

Since the profiles are symmetric, only half-profiles are plotted with in-plane profiles along the negative direction and cross-plane profiles along the positive direction.

The phantom geometry is altered to make the calculation plane sensitive to the thickness of added backscatter. This is achieved by using a 1 cm thick build-up slab with a density of 0.18 g/ cm3 and by centering the calculation plane in the sheet of voxels, which comprise the exit surface of the build-up slab.

3.6.3 Target matrix

A grey-scale image of the target matrix is illustrated in Fig. 3-5 (a), while a colored surface plot representation is provided in Fig. 3-5(b).

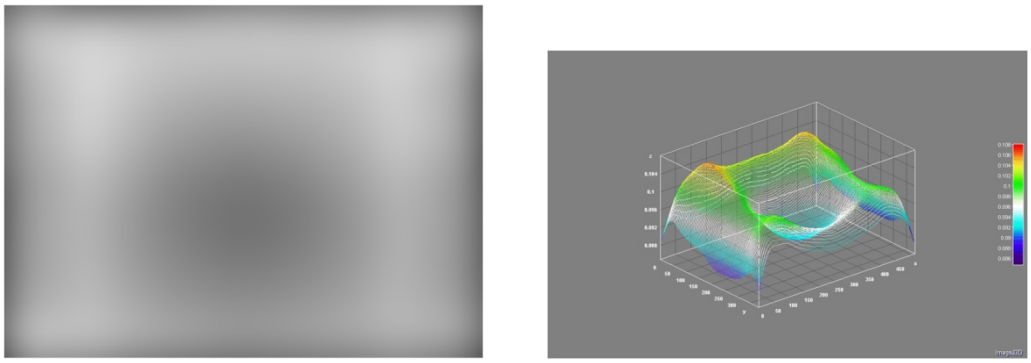

a) b)

Figure 3-5: Target matrix (a) greyscale image (b) surface plot

The Gaussian blur filter was necessary to eliminate the appearance of stripe artefacts arising from its construction. The effect of the support arm is to boost the dose across the width of the EPID over about two-thirds of the EPID area closest to the gantry when irradiated with a flood field. Pixel variation in this matrix is due to both horns in the flood-field and to non-uniform backscatter, but the observed in-plane asymmetry of the central axis in-plane profile of about 7.5% is attributed to non-uniform backscatter.

3.6.4 Backscatter ROI

The resulting backscatter ROI is shown in Fig. 3-6. The shape of the ROI can be seen to roughly follow the expected backscatter material of the support arm.

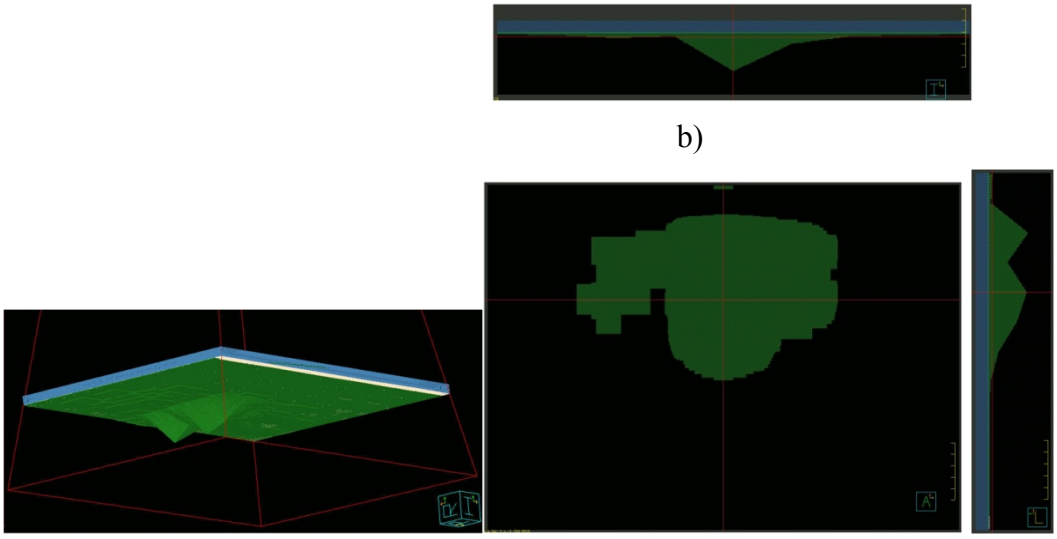

b)

a) c) d)

Figure 3-6: Perspective view (a), axial section (b), coronal section (c) and sagittal section (d) through the ROI constructed to model backscatter from the EPID support-arm.

The bulk of the ROI is oriented along the in-plane direction (Y axis) and its thickness drops to zero far from the gantry. The thin, "residual", ROI thickness present far from the Y axis and the "appendage" that can be seen on the coronal view are consistent with the presence of cross bars and folded cables in the EPID.

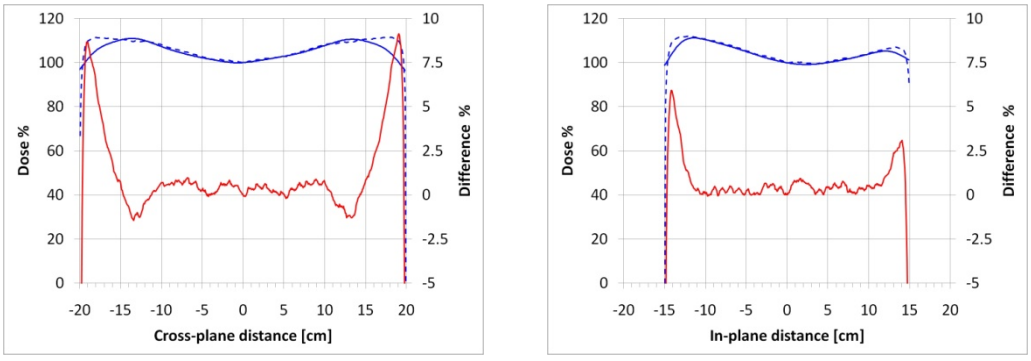

a) b)

Figure 3-7: Comparison of axial beam profiles for the TM (solid blue line) and P(FF) (dashed blue line) in the x (cross-plane) direction (a) and y (in-plane) direction (b). The axis on the right refers to the percent difference plotted as a solid red line.

The axial profiles of the TM and TPS-calculated flood field, P(FF), are shown in Fig. 3-7. P(FF) follows closely the TM, as required by eq. (3.8), in the central (30 x 30 cm^2) part of the EPID. The increased errors towards the periphery can be attributed to the fact that the sought-for TM has lower values there than the TPS flood-field dose. Such a situation cannot be corrected by the addition of backscatter material, as that can only increase the dose in any given region.

3.6.5 Results for Representative Fields

Corrected TPS planar dose maps are compared to feature-restored EPID images for various square and rectangular fields from 5 to 30cm. Step and shoot IMRT test patterns resembling a well, a tower and a step-wedge are also tested. Results are plotted in figures 3-8 to 3-12.

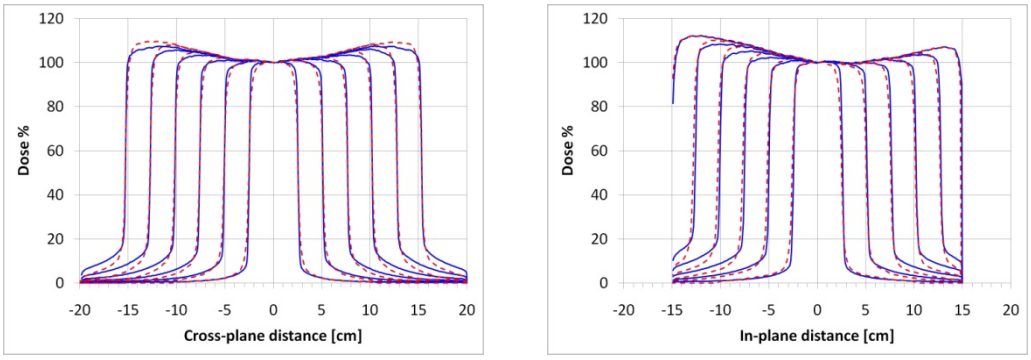

a) b)

Figure 3-8: Comparison of axial beam profiles for square fields in the x (cross-plane) direction (a) and y (in-plane) direction (b). Solid lines represent EPID data and dashed lines represent TPS data.

Figure 3-8 shows the axial profiles for the square fields. It shows good agreement between the TPS-calculated planar dose maps and feature-restored EPID images. For the

30 cm square field, the in-plane profiles of the TPS dose and EPID image are, as expected, quasi-identical since those profiles are, for any practical purpose, identical to the y profiles of a flood field, the latter being the field used to design the backscatter ROI. For all fields, profile shoulders calculated by Pinnacle[3] are slightly more rounded than those of the EPID images.

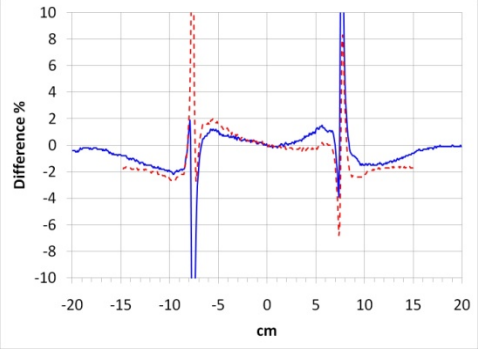

Figure 3-9: Percent difference plotted for the X and Y profiles of a 15x15 cm^2 square field, which is representative of the other field sizes as well.

The solid blue line corresponds to the X profile and the dashed red line corresponds to the Y profile.

Figure 3-9 shows differences between the TPS planar dose and EPID image for a 15 x 15 cm^2 field, which are representative of the errors seen for other fields as well.

Figure 3-10 shows results for a 6 x 15 cm^2 field. The x profiles are similar to the x-profiles for a 6-cm square field and the y profiles are similar to the y profiles of a 15-cm square field.

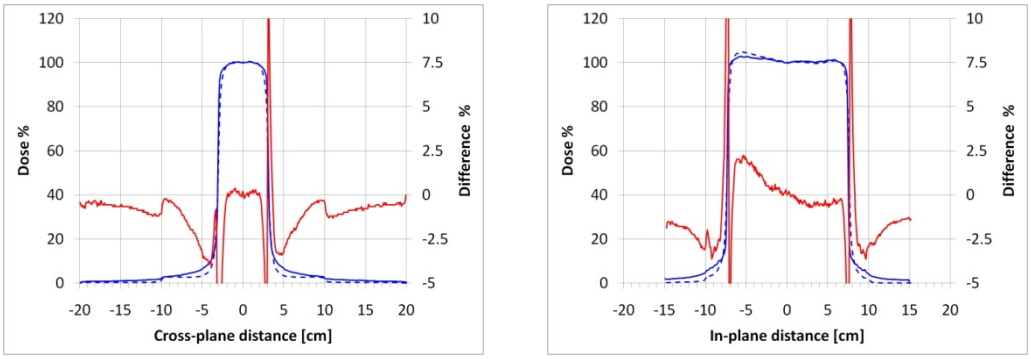

a) b)

Figure 3-10: Comparison of axial beam profiles for a 6x15 cm^2 rectangular field in the x (cross-plane) direction (a) and y (in-plane) direction (b).

The solid blue line represents EPID data, while the dashed blue line represents TPS data. The axis on the right refers to the percent difference plotted as a solid red line.

Results for a square well are shown in Fig. 3-11 for the cross-plane direction at y=0 cm and for the in-plane direction at x=0 cm and x = 5 cm. The plots show that the TPS dose agrees well with the EPID in predicting the relative height of dose peaks. Figures 3-11-a and 3-11-b show that the lower values of the peaks closer to the gantry are well captured by the TPS. Comparing Figs. 3-11-b and 3-11-d, it can also be seen that the relative height of the peaks corresponding to the red zone on the dose map (100%) and the yellow zone on the dose map (70%) is also well captured by the TPS. The results for a step-wedge field are shown in Fig. 3-12. There is reasonably-good agreement between the EPID image and the TPS dose. The step wedge is programmed to deliver equal monitor units to a sequence of successively narrower MLC-shaped rectangles. Therefore, the strips corresponding to lower dose are exposed by relatively wider fields than those corresponding to higher doses. The effective field size appears to influence the agreement

between imaged and calculated profiles. Notice that successive steps in the X profile of Fig 3-12 (b) fall faster for the Pinnacle[3] calculation than for the EPID image.

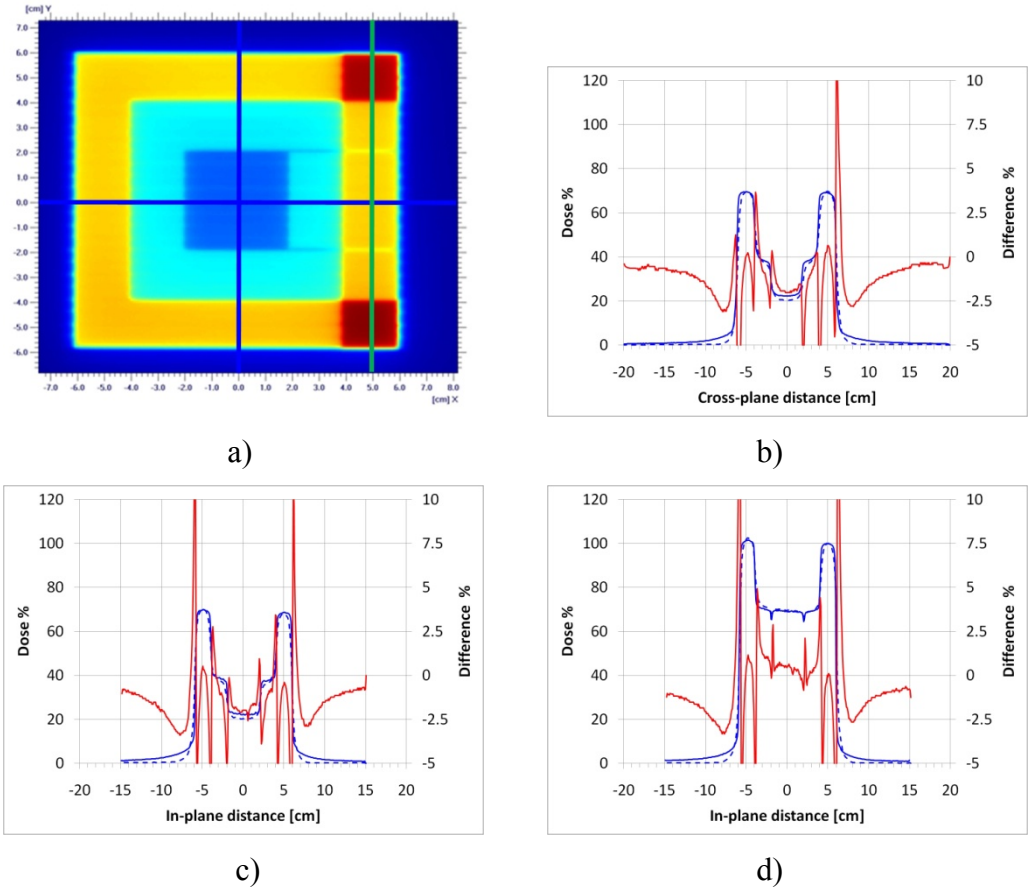

Figure 3-11: Comparison of axial beam profiles for a Well field (a) in the x (cross-plane) direction (b) and y (in-plane) direction at x=0 (c) and x=5cm (d)

The solid blue line represents EPID data, while the dashed blue line represents TPS data. The axis on the right refers to the percent difference plotted as a solid red line.

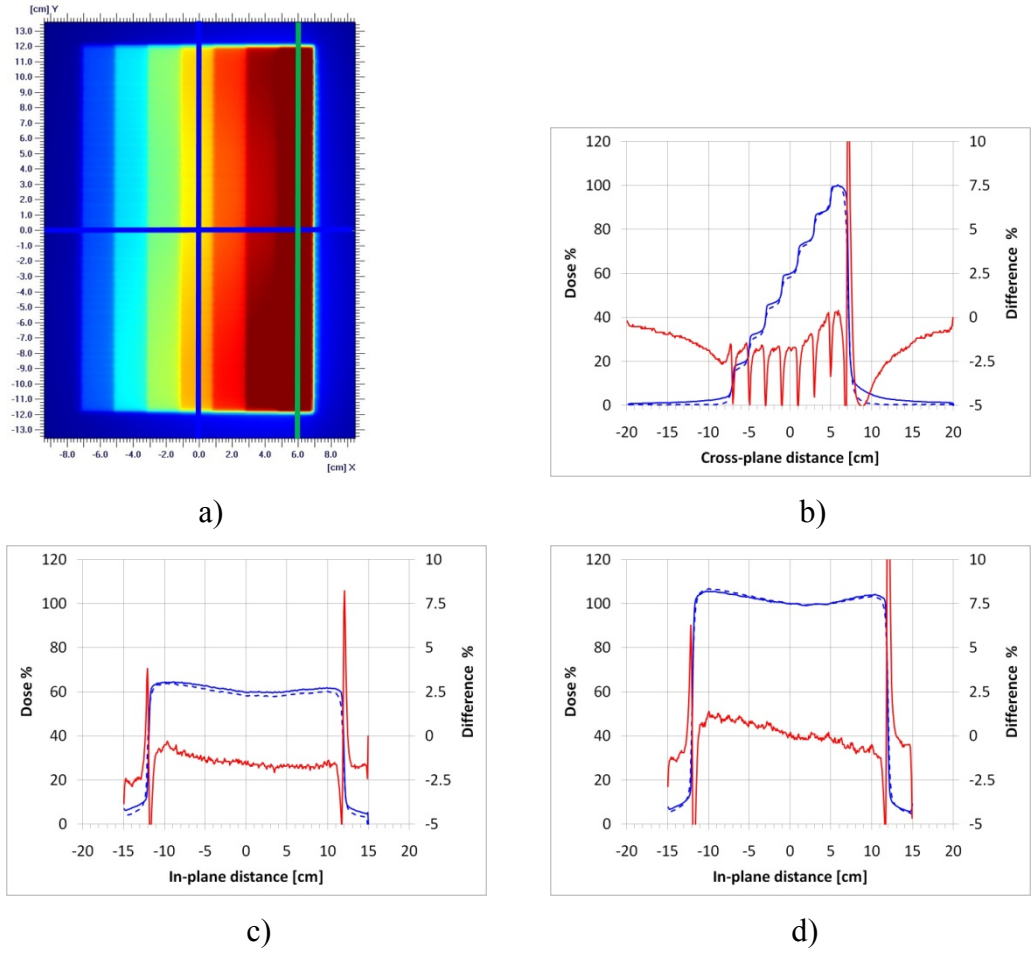

Figure 3-12: Comparison of axial beam profiles for a Step-Wedge field (a) in the x (cross-plane) direction (b) and y (in-plane) direction at x=0 (c) and x=6cm (d)

The solid blue line represents EPID data, while the dashed blue line represents TPS data. The axis on the right refers to the percent difference plotted as a solid red line.

3.7 Results Interpretation / Discussion

All fields show reasonable overall agreement between the calculated and measured profiles. For all fields, profile shoulders calculated by Pinnacle[3] are slightly more rounded than those of the EPID images. This is more evident for the X profiles since they are more symmetric. Because this error is present in all fields, it is likely due to

mistuned Pinnacle^3 model parameters and to EPID scatter and glare, which are not accounted for in the Pinnacle^3 model. The latter explanation seems to be supported by the fact that a fitted scatter and glare kernel obtained using the method outlined in chapter 4 (Nichita, Ostapiak & Farrell, 2011) substantially improves agreement of the x profile for the 20 x 20 cm^2 and 25 x 25 cm^2 fields, as shown in Fig. 3-13.

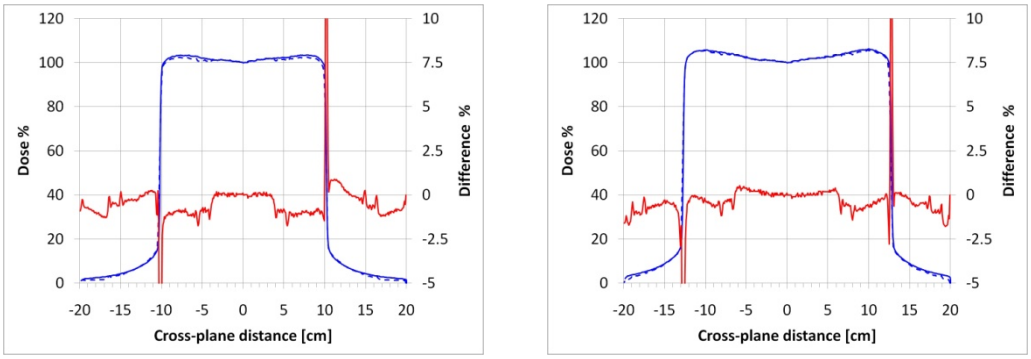

a) b)

Fig. 3-13. Comparison of cross-plane axial beam profiles for a 20x20 cm^2 (a) and a 25x25 cm^2 (b) square field obtained using a fitted scatter and glare kernel. The solid blue line represents EPID data, while the dashed blue line represents TPS data. The axis on the right refers to the percent difference plotted as a solid red line.

The in-plane profiles of Pinnacle^3 dose maps, with the exception of the 30cm x 30 cm are somewhat more asymmetric (have higher values towards the gantry) than the corresponding EPID profiles. This is most evident for the 20x20 cm^2 and 25x25 cm^2 square fields. This is likely due to insufficient backscatter at angles less than 180° in the Pinnacle^3 model. Consequently, the backscatter component of the dose at a point on the dose-plane arises from a volume of the backscatter region that is closer to the point than that for the actual EPID. This has the effect of reducing the field-size dependence of

backscatter in the Pinnacle^3 model, which, in turn, results in less backscatter reduction as the field size is decreased from 30cm x 30 cm (where agreement is excellent by design) and hence a higher TPS-predicted response towards to the gantry.

As mentioned in section 3.6, results for the step wedge show that the effective field size influences the agreement between imaged and calculated profiles. Successive steps in the X profile of Fig. 3-12 (b) increase faster for the Pinnacle^3 calculation than for the EPID image. This is consistent with the supposition that the Pinnacle^3 model is relatively insensitive to non-local backscatter compared to the EPID, since the increase in monitor units delivered to successively smaller steps would otherwise be offset by a slight decrease in relative non-local scatter due to the smaller field size. In other words, a greater dependence of Pinnacle^3 model dose on field size would result in better overall agreement.

4 Modelling Scatter, Glare and Increased Off-Axis Response

4.1 Approach

As mentioned in the introduction, one of the challenges associated with EPIDs is the fact that the generated image does not follow directly the energy fluence but is blurred due to X-ray photon scattering as well as to light-photon scattering (glare). As a result, the generated image, I is, in the general case, related to the fluence, Ψ by a position-dependent Point Spread Function (PSF), or kernel:

$$I(\vec{r}) = \int \psi(\vec{r}\,')k(\vec{r},\vec{r}\,')d^2\vec{r}\,' \tag{4.1}$$

The PSF is also implicitly dependent on the X-ray photon energy spectrum at each point. The PSF itself can be assumed to be a convolution of two or more position dependent or translation-invariant kernels. Usually, continuous representations of the PSF are used, representations that provide values for the PSF at any point in the EPID plane. However, the EPID image itself corresponds to a discrete pixel grid. The reading for a pixel located at $\vec{r}_{i,j}$ is:

$$I_D(i,j) \equiv I(\vec{r}_{i,j}) \tag{4.2}$$

Given the discrete nature of the EPID image grid, it is of interest to write a spatially-discrete form of eq. (4.1):

$$I_D(i,j) = \sum_{i',j'} \psi(i',j')k(i,j,i',j') \tag{4.3}$$

An interesting problem is to find $k(i,j,i',j')$ based only on measurements, without resorting to Monte Carlo simulations. As a first step, the discrete kernel can be found for the simple case when the kernel is translation- and rotation-invariant, that is dependent only on the distance between the pixels *(i,j)* and *(i',j')*:

$$k(i,j,i',j') = k\left(\sqrt{(i-i')^2 + (j-j')^2}\right) \tag{4.4}$$

For such a simplified function, eq. (4.3) transforms into a convolution (denoted by the $\otimes$ symbol):

$$I_D(i,j) = \sum_{i',j'} \psi(i',j') k(i-i', j-j') \equiv (\psi \otimes k)(i,j) \tag{4.5}$$

Since the image is discretized pixel-by-pixel, the kernel values are also sought on a discrete set of points, namely:

$$k_n \equiv k(n) = k(\text{int}[\sqrt{\xi^2 + \eta^2} + 0.5]) \tag{4.6}$$

where *n* represents the integer distance in pixels (assumed square) from the interaction site to the scoring site and $(\xi,\eta) \equiv (i-i', j-j')$ represents the relative position of the scoring pixel with respect to the interaction pixel. It follows that the two-dimensional kernel can be written as a linear combination:

$$k(\xi,\eta) = \sum_{n=0}^{N} k_n \phi_n(\xi,\eta) \tag{4.7}$$

where the functions $\phi_n(\xi,\eta)$ are defined to be zero everywhere except on a discrete Cartesian approximation of an annulus of inner radius n-0.5 and outer radius n+0.5 (disk of radius 0.5 for n=0), that is:

$$\phi_n(\xi,\eta) = \delta\left(n, \text{int}[\sqrt{\xi^2+\eta^2}+0.5]\right) \tag{4.8}$$

where δ is the Kronecker Delta symbol. In practice, N is taken to be large-enough so that the kernel becomes negligibly small at that distance. The coefficients k_n are found using a simple least-squares method, where the function to be minimized is:

$$\Omega = \sum_{i,j}\left(I_D(i,j) - \sum_{n=0}^{N} k_n \left(\psi \otimes \phi_n\right)(i,j)\right)^2 \tag{4.9}$$

In the above equation, the convolution symbol, $\otimes$, has the same meaning as in equation (4.5). By requiring the derivative with respect to each k_n to vanish, the minimization of the function expressed by eq. (4.9) translates into the linear system:

$$\sum_{n=0}^{N} k_n \left\{ \sum_{i,j}\left[\left(\psi \otimes \phi_n\right)(i,j)\right]\left[\left(\psi \otimes \phi_m\right)(i,j)\right]\right\} = \sum_{i,j} I_D(i,j)\left[\left(\psi \otimes \phi_m\right)(i,j)\right] \tag{4.10}$$

The values k_n are found by solving the linear system in Eq. (4.10).

The kernel expansion in eq. (4.7) can be improved by using fewer radial functions than N, the number of radial pixels used to represent the kernel.

The kernel can be expressed using a different set of functions, $\varphi_n(\xi,\eta)$

$$k(\xi,\eta) = \sum_{n=0}^{N'<N} k_n \varphi_n(\xi,\eta) \tag{4.11}$$

Each function is defined to be piecewise linear:

$$\varphi_n(\xi,\eta)=\varphi_n(r)=\begin{cases}\dfrac{r-r_{n-1}}{r_n-r_{n-1}} \text{ for } r_{n-1}<r<r_n\\ \dfrac{r_{n+1}-r}{r_{n+1}-r_n} \text{ for } r_n<r<r_{n+1}\end{cases} \tag{4.12}$$

This is illustrated in Fig. 4-1 for a six-function expansion.

Figure 4-1: Position-Invariant Kernel Expansion

To account for the spatial dependence of the kernel, induced by the off-axis softening, a more complicated expression than eq. (4.7) is needed. One way to account for the position dependence of the kernel is to assume that the shape of the kernel depends explicitly on the interaction point while still preserving azimuthal symmetry, that is:

$$k(r',r)=k(r',|r'-r|) \tag{4.13}$$

where the prime denotes incidence point and the non-prime denotes the scoring point. Of course, such a kernel is not symmetric. The interaction and scoring points are not interchangeable anymore.

To simplify things, it can be assumed that for each interaction point the kernel is a linear combination of azimuthally symmetric kernels:

$$k(r',r)=\sum_{p}h_p(r')k_p(|r-r'|) \tag{4.14}$$

Using the same functions $\varphi_n(|r-r'|)$ as before for the radial dependence, the following is obtained for a kernel with incidence at the origin:

$$k_p(|r-r'|)=\sum_{k=1}^{n}c_{pk}\varphi_k(|r-r'|) \tag{4.15}$$

It follows that the overall kernel is equal to:

$$k(r',r)=\sum_{p}h_p(r')\sum_{k=1}^{n}c_{pk}\varphi_k(|r-r'|) \tag{4.16}$$

Determining the kernel is equivalent to finding coefficients c_{pk}.

Following the same reasoning as for the translation-invariant kernel, the resulting system is found to be:

$$\sum_{p,k}c_{pk}\left\langle\left(\Psi h_p\right)\otimes\varphi_{pk};\left(\Psi h_q\right)\otimes\varphi_{ql}\right\rangle=\left\langle EPID;\left(\Psi h_q\right)\otimes\varphi_{ql}\right\rangle \tag{4.17}$$

In the above equation, the convolution symbol, $\otimes$, has the same meaning as in equation (4.5). As a reminder, when using a translation-invariant kernel, a simpler equation, eq. (4.10), applies.

Functions h_p can be chosen to be similar in shape to the functions used to expand the translation-invariant kernel, that is

$$h_p(r) = \begin{cases} \dfrac{r - r_{n-1}}{r_n - r_{n-1}} \; for \; r_{n-1} < r < r_n \\ \dfrac{r_{n+1} - r}{r_{n+1} - r_n} \; for \; r_n < r < r_{n+1} \end{cases} \tag{4.18}$$

The kernel dependence on the distance between the axis and interaction point is shown in fig. 4-2.

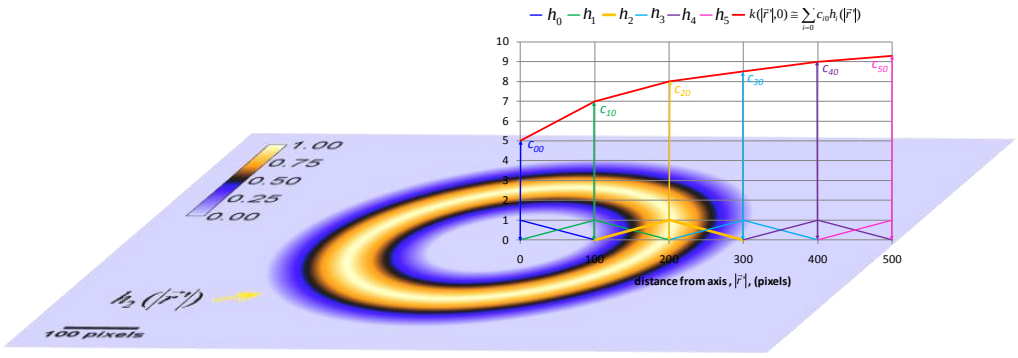

Figure 4-2: Kernel Dependence on Distance from Axis to Interaction Point

The notable difference between eq. (4.18) and eq. (4.12) is that whereas in eq. (4.12) the radius represents the distance between the interaction and scoring point, in eq. (4.18) r represents the distance between the scoring point and the center of the field.

4.2 Results

4.2.1 Position-Invariant Kernel

The kernel based on translation-invariant functions defined by eq. (4.11) was tested using a simulated fluence obtained from a simulated, perfectly uniform, rectangular field, 200 by 100 pixels, (Fig. 4-3-a) convolved with a pillbox kernel 5 pixels in diameter (Fig. 4-3-b) to simulate the penumbra. Transmission through the collimator and in-field fluence variations were ignored. The resulting fluence map is shown in Fig. 4-3-c. The EPID image was simulated by convolving the fluence with a simple, linearly decreasing PSF with a radius equal to 20 pixels ($k_n = 21 - n$). The two-dimensional PSF is shown in Fig. 4-3-d and the resulting simulated EPID image is shown in Fig. 4-3-e.

a) b) c) d) e)

Figure 4-3: Simulated Fluence Map and EPID Image

As a first test, the algorithm was applied to find the PSF based on the image and fluence map. As expected, the calculated PSF was identical to the one that was used to generate the image and thus the algorithm was shown to function correctly. Recognizing that, in reality, the fluence can only be determined approximately due to measuring errors, a second test was performed. For this second test, a "measured" fluence was simulated by applying a random "measurement error", uniformly distributed in the (-10%, +10%)

interval, to the true fluence. The corresponding, "measured", PSF was calculated by using the true image and the "measured" fluence as inputs to the algorithm. The "measured" PSF was found to differ slightly from the PSF used to generate the image. The difference can be seen in Fig. 4-4, which shows plots of both PSFs.

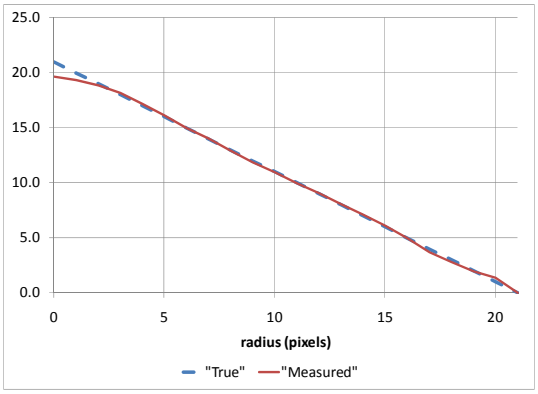

Figure 4-4: Plot of "True" PSF and PSF determined from a "Measured" EPID Image

The "measured" PSF was subsequently convolved with the true fluence and the result compared with the "true" image. The difference map is shown in Fig. 4-5-a and the profile of the percent difference (calculated relative to the maximum pixel value in the image) is shown in Fig. 4-5-b. It can be seen that the maximum error is below 0.1% of the central axis value even in the large-gradient region.

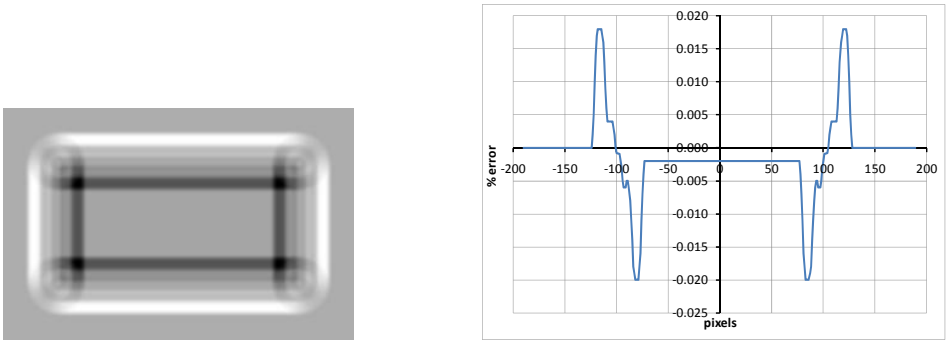

a) b)

Figure 4-5: Differences between Actual Image and Image Reconstructed using the PSF based on the "Measured" EPID Image

To test the ability of the kernel obtained from one field shape to reproduce EPID readings for other field shapes, the following numerical experiment was performed. A checkerboard fluence, shown in Fig. 4-6-a, and its corresponding simulated EPID image, shown in Fig. 4-6-b, were used to find the coefficients multiplying the basis functions of the linear expansion used to represent the kernel. The fluence was simulated as a plain checkerboard mask, convolved with a disk kernel to simulate the geometric penumbra (same as before). The EPID image was simulated by convolving the fluence with a triple-exponential kernel representing both high-energy scatter and glare, as described by Kirkby (2005):

$$k(r) = e^{-P_1 r} + P_2 e^{-P_3 r} + P_4 e^{-P_5 r} \qquad (2.1)$$

The number of basis functions, of the type defined by eq. (4.12), used to represent the kernel was 6.

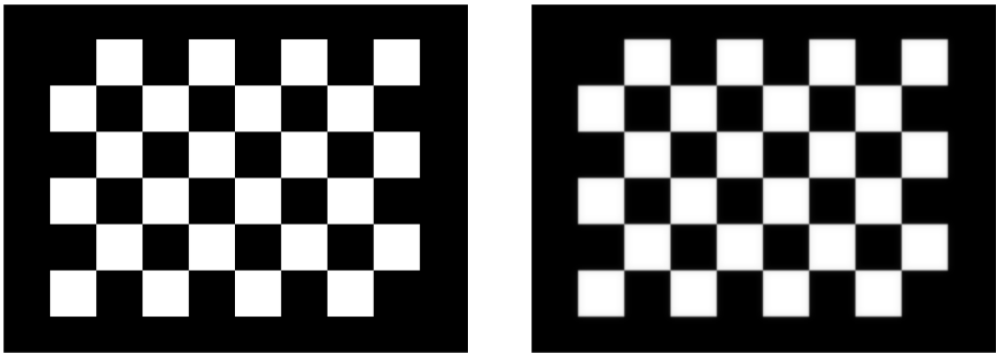

a) b)

Figure 4-6: Checkerboard Fluence (a) and EPID Image (b)

The resulting translation-invariant kernel is shown in Fig. 4-7-a and the % error in map is shown in Fig. 4-7-b. As can be seen, the fit is very good.

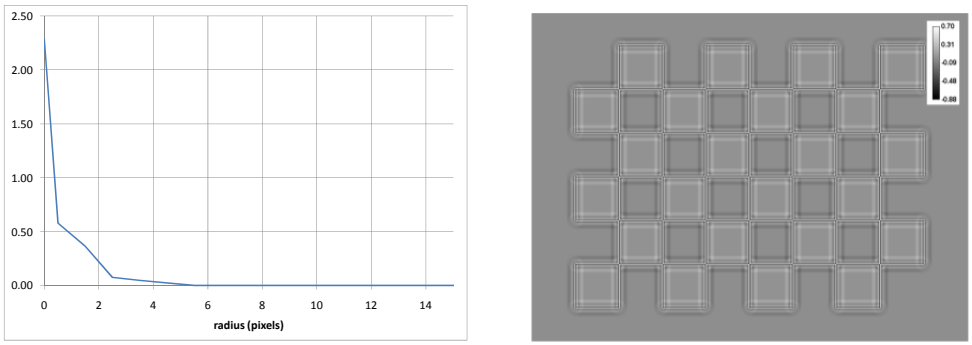

a) b)

Figure 4-7: Translation-Invariant Kernel (a) and % Error Map (b)

To test the obtained kernel for different fluence patterns, an 4.5cm x 4.5cm IMRT-field fluence was simulated, as shown in Fig. 4-8-a. It was then convolved with the same exponential kernel documented in the literature to obtain the corresponding EPID image shown in Fig. 4-8-b.

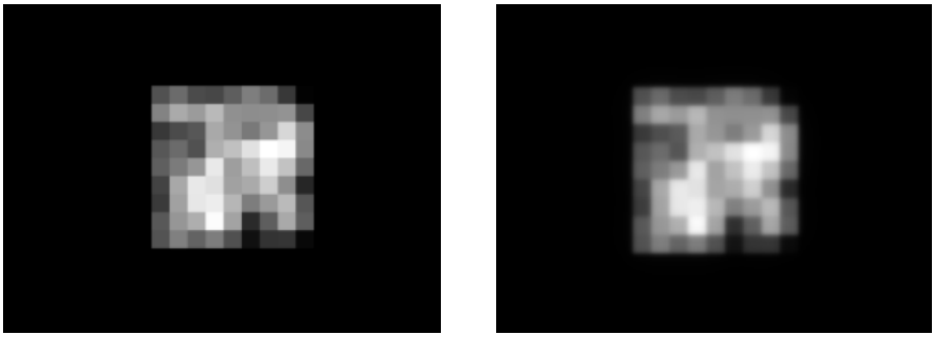

a) b)

Figure 4-8: Simulated IMRT Fluence (a) and EPID Image (b). The scale of the images may be inferred from the 5 mm pixel dimension.

When applying the kernel calculated using the checkerboard pattern to the IMRT fluence, the EPID image was reproduced very well, as shown by Fig. 4-9, which shows the % error in reproducing the IMRT EPID image.

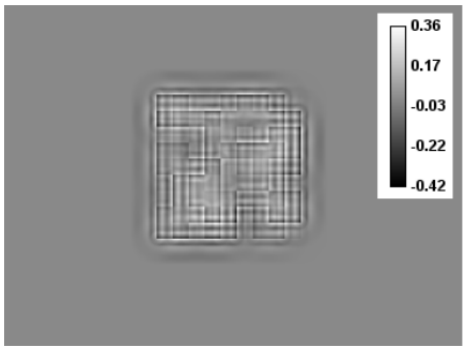

Figure 4-9: % error map in reproducing the IMRT-field EPID image.

This demonstrates that the calculated kernel does a good job of reproducing fields other than the one used to calculate it.

4.2.2 Position-Dependent Kernel

To investigate what happens when the EPID response becomes position dependent due to radial beam softening, an "energy-horns" (or "e-horns") mask was superimposed onto (multiplied by) the fluence to simulate the EPID's variable sensitivity to photon energy. The mask was represented as an inverted cone of height 20%. It is shown in Fig. 4-10 and the resulting EPID checkerboard image is shown in Fig. 4-11-a. Fig. 4-11-a does not appear to differ from Fig. 4-6-b by eye, but a profile plot (Fig. 4-11-b) shows the amplitude variation.

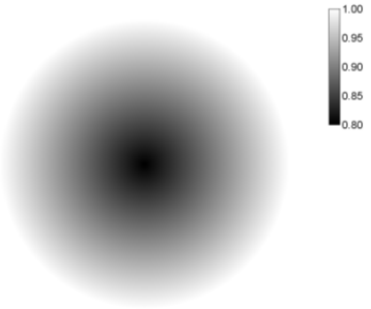

Figure 4-10: Energy "Horns"

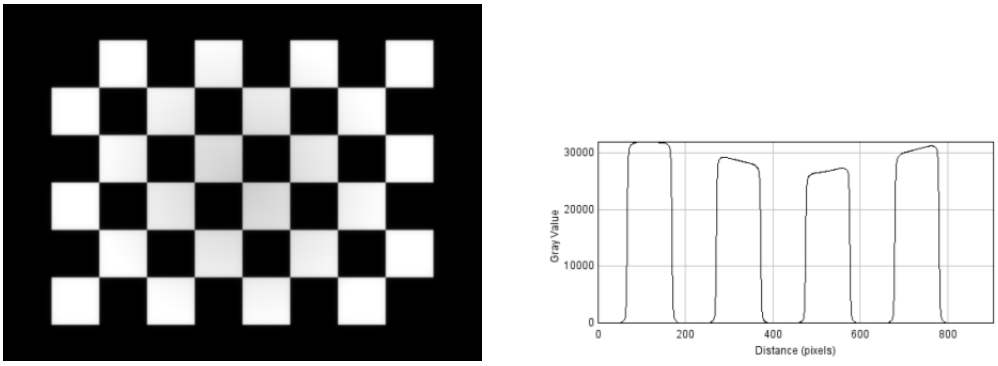

a) b)

Figure 4-11: Checkerboard EPID image with energy-dependent response (a) and profile plot (b)

For testing resulting kernels on a different field, a larger, 8.5cm x 8.5 cm IMRT field was simulated. A larger field was used so that the differences induced by beam softening become significant. A small field may be insensitive to small variations in sensitivity. The IMRT field is shown in Fig. 4-12.

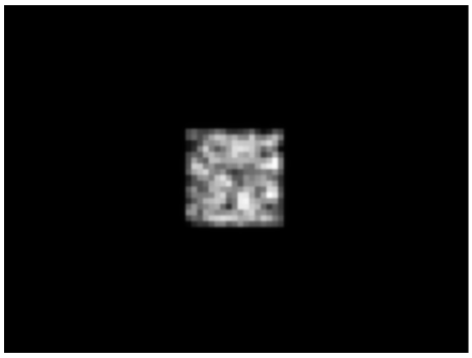

Figure 4-12: EPID image of the IMRT field

Regarding the position-dependence of the kernel due to radial beam softening, the first thing that needs to be checked is whether a translation-invariant kernel determined by trying to transform Fig. 4-6-a into Fig. 4-11-a can do a reasonable job of reproducing Fig. 4-11-a. The resulting translation-invariant kernel may not resemble the true kernel used in conjunction with the e-horns to obtain Fig. 4-11-a, but it would be still acceptable, especially if it could be used successfully for other fields, such as IMRT fields similar to the one in fig. 4-12. To test this, a translation-invariant kernel was calculated and then used for both the checkerboard and the IMRT fields. The % errors are shown in Fig. 4-13-a and 4-13-b respectively.

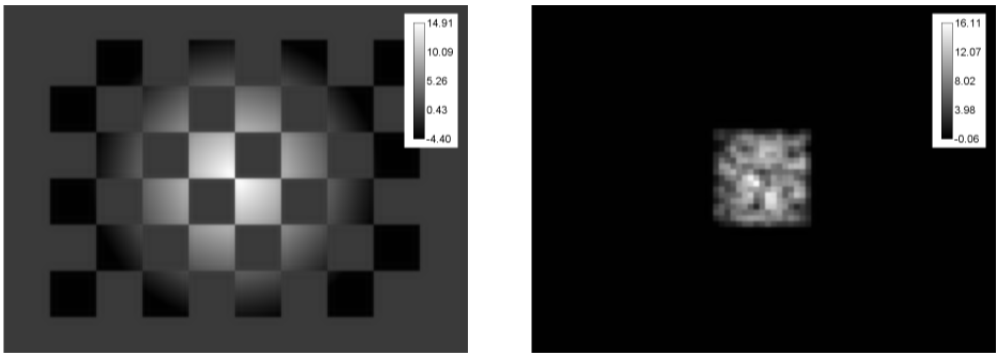

a) b)

Figure 4-13: % error when reproducing the checkerboard field (a) and IMRT field (b)

It is clear from fig. 4-13 that a position-invariant kernel does not properly account for the variation in sensitivity induced by beam softening, at least not to the degree (20%) this effect was simulated in the test cases.

To account for such spatial dependence of the kernel, a kernel depending explicitly on the distance between the axis and interaction point, as expressed by eq. 4-14 was subsequently used.

When applying the new, non-translation invariant kernel, the errors in representing the checkerboard field as well as the IMRT field were greatly reduced, as shown in fig. 4-14-a and fig. 4-14-b. It will be noted that the same kernel calculated using the checkerboard field was also used for the simulated IMRT field.

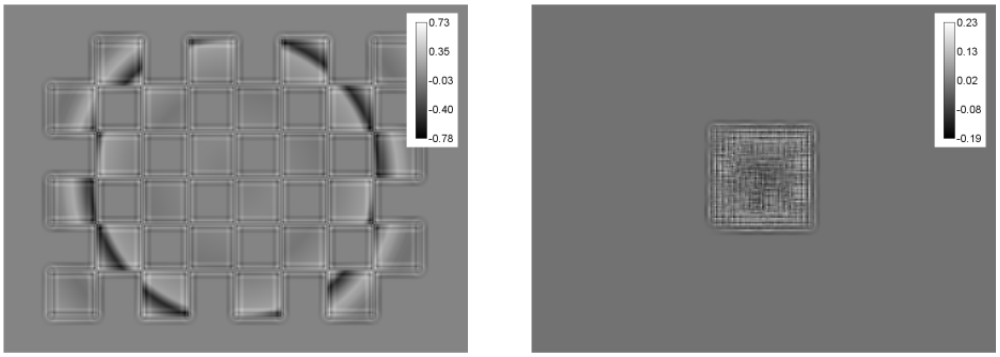

a) b)

Figure 4-14: % error in reproducing the checkerboard field (a) and IMRT field (b) using a non-translation-invariant kernel

5 Conclusions and Future Work

5.1 Backscatter

A novel method for IMRT QA was developed whereby TPS-calculated planar dose maps are compared to feature-restored EPID images. The TPS model geometry incorporates a region of non-uniform thickness that backscatters dose to the calculation plane. This region is designed so that the TPS flood-field planar-dose matches the corresponding "target matrix", which represents the flood-field EPID dose or, equivalently, a corrected flood-field EPID image that would be obtained if the correction image consisted only of pixel sensitivity, with no "horns" or support-arm backscatter. The TM is approximated using a novel technique that infers the EPID response to backscatter based on slit-field corrected images, which depend on backscatter only through the flood-field correction. The method is easy to commission and use in clinical practice and does not require measurements involving the removal of the EPID from the support-arm. Slight discrepancies between the Pinnacle^3 calculations and EPID response are attributed to sub-optimally tuned parameters in the Pinnacle^3 model.

5.2 Scatter, Glare and Off-Axis Response

The new method developed for calculating position-dependent kernels seems to be very successful in reproducing simulated EPID images based on fluence maps. As a practical issue, the fluence maps can be replaced by planar dose maps calculated using the TPS.

The position-dependent kernel can then be applied to the TPS dose map and the result compared to the EPID image. It is to be noted that amplitudes are included in the kernels, so the absolute EPID readings are found using this method. Therefore no additional calculations are needed to normalize the computed EPID images.

5.3 Future Work

Methods to extend the range of backscatter in the current TPS model may be explored in order to test the hypothesis (stated at the end of Section 3.7) that a greater dependence of backscatter on field size in the TPS model would improve agreement between calculated and acquired EPID images. Developing a method that combines the modelling of non-uniform backscatter with the modelling of scatter, glare and off-axis response promises to improve agreement between the TPS-calculated EPID response and the actual EPID response.

References

1. Antonuk, L.E. et al., 1998. Initial performance evaluation of an indirect-detection, active matrix flat-panel imager (AMFPI) prototype for megavoltage imaging. Int. J. Radiat. Oncol. Biol. Phys. 42, 437-454
2. Antonuk, L.E., 2002. Electronic portal imaging devices: a review and historical perspective of contemporary technologies and research. Phys. Med. Biol. 47, R31–R65
3. Berry, S.L., Polvorosa, C.S., Wuu, C.S., 2010. A field size specific backscatter correction algorithm for accurate EPID Dosimetry. Med. Phys. 37, 2425-2434.
4. Budgell, G.J. et al., 2005. Improving IMRT quality control efficiency using an amorphous silicon electronic portal imager. Med. Phys. 32, 3267-3278.
5. Cufflin, R.S. et al., 2010. An investigation of the accuracy of Monte Carlo portal dosimetry for verification of IMRT with extended fields. Phys. Med. Biol. 55, 4589-4600.
6. El-Mohri, Y. et al., 1999. Relative dosimetry using active matrix flat-panel imager (AMFPI) technology. Med. Phys. 26, 1530-1541.
7. Epperson, J.F., 2002. An Introduction to Numerical Methods and Analysis. 151-152. John Wiley and Sons

8. Greer P.B., Popescu C.C., 2003. Dosimetric properties of an amorphous silicon electronic portal imaging device for verification of dynamic intensity modulated radiation therapy. Med. Phys. 30, 1618-1627

9. Greer, P.B., 2005. Correction of pixel sensitivity variation and off-axis response for amorphous silicon EPID dosimetry. Med. Phys. 32, 3558-3568

10. Greer, P.B, Vial, P., Oliver, L., Baldock, C., 2007. Experimental investigation of the response of an amorphous silicon EPID to intensity modulated radiotherapy beams. Med. Phys. 34, 4389-4398

11. Greer, P.B. et al., 2009. An energy fluence-convolution model for amorphous silicon EPID dose prediction. Med. Phys. 36, 547-555

12. Grein, E.E., Lee, R., Luchka, K., 2002. An investigation of a new amorphous silicon electronic portal imaging device for transit dosimetry. Med. Phys. 29, 2262-2268

13. Kawrakow, I. & Rogers, D. W., 2002. The EGSnrc Code System: Monte Carlo Simulation of Electron and Photon Transport, NRCC Report, PIRS-701, NRC Canada.

14. Khan, R.F.H., Ostapiak, O.Z., Szabo, J.J., 2008. An empirical model of electronic portal imager response implemented within a commercial treatment planning system for verification of intensity-modulated radiation therapy fields. J. App. Clin. Med. Phys. 9, 135-150

15. Kirkby, C., Sloboda, R., 2005. Comprehensive Monte Carlo calculation of the point spread function for a commercial a-Si EPID. Med. Phys. 32, 1115-1127„

16. Ko, L., Kim, J.O., Siebers, J.V., 2004. Investigation of the optimal backscatter for an aSi electronic portal imaging device. Phys. Med. Biol. 49, 1723-1738

17. Li, W., Siebers, J.V., Moore, J.A., 2006. Using fluence separation to account for energy spectra dependence in computing dosimetric a-Si EPID images for IMRT fields. Med. Phys. 33, 4468-4480

18. McCurdy, B.M., Luchka, K., Pistorius, S., 2001. Dosimetric investigation and portal dose image prediction using an amorphous silicon electronic portal imaging device. Med. Phys. 28, 911-924

19. McDermott, L.N. et al, 2004. Dose–response and ghosting effects of an amorphous silicon electronic portal imaging device. Med. Phys. 31, 285–295

20. McDermott, L.N. et al., 2006. Comparison of ghosting effects for three commercial a-Si EPIDs. Med. Phys. 33, 2448-2451.

21. Moore, J. A., Siebers, J. V., 2005. Verification of the optimal backscatter for an aSi electronic portal imaging device. Phys. Med. Biol. 50, 2341-2350

22. Nichita, E., Ostapiak, O. & Farrell, T., 2011. Position-Dependent Discrete Point Spread Functions for EPID IMRT QA, Proc. Joint COMP/AAPM Annual Meeting, Vancouver BC July 31- August 4

23. Nicolini, G. et al., 2006. GLAaS: An absolute dose calibration algorithm for an amorphous silicon portal imager. Applications to IMRT verifications. Med. Phys. 33, 2839-2851

24. Nicolini G. et al., 2008. Testing the GLAaS algorithm for dose measurements on an amorphous silicon portal imager on low and high energy photon beams. Med. Phys. 35, 464-472

25. Nicolini, G. et al., 2008. Testing the portal imager GLAaS algorithm for machine quality assurance. Rad. Onc. 3:14

26. Nicolini, G. et al., 2008. The GLAaS algorithm for portal dosimetry and quality assurance of RapidArc, an intensity modulated rotational therapy. Rad. Onc. 3:24

27. Parent, L. et al., 2006. Monte Carlo modelling of a-Si EPID response: The effect of spectral variations with field size and position. Med. Phys. 33, 4527-4540

28. Partridge, M. et al., 2010. A study of the spectral response of portal imaging detectors. Proceedings of the IEEE Nuclear Science Symposium

29. Podgorsak, E.B. (technical editor), 2005. Radiation Oncology Physics: A handbook for Teachers and Students. IAEA

30. Rowshanfarzad, P. et al., 2010. Measurement and modeling of the effect of support arm backscatter on dosimetry with a Varian EPID. Med. Phys. 37, 2269-2278

31. Rowshanfarzad, P. et al., 2010. Reduction of the effect of non-uniform backscatter from an E-type support arm of a Varian a-Si EPID used for dosimetry. Phys. Med. Biol. 55, 6617-6632.

32. Siebers, J.V. et al., 2004. Monte Carlo computation of dosimetric amorphous silicon electronic portal images. Med. Phys. 31, 2135-2146

33. Siewerdsen, J.H., Jaffray, D.A., 1999. A ghost story: spatio-temporal response characteristics of an indirect-detection flat-panel imager. Med. Phys. 26, 1624-1641.

34. Steciw, S. et al., 2005. Three-dimensional IMRT verification with a flat-panel EPID. Med. Phys. 32, 600-612

35. Talamonti, C,, Casati, M., Bucciolini, M., 2006. Pretreatment verification of IMRT absolute dose distributions using a commercial a-Si EPID. Med. Phys. 33, 4367-4378

36. Van Elmpt, W. et al., 2008. A literature review of electronic portal imaging for radiotherapy dosimetry. Radiotherapy and Oncology 88, 289-309

37. Van Esch, A., Depuydt, T., Huyskens, D. P., 2004. The use of an aSi-based EPID for routine absolute dosimetric pre-treatment verification of dynamic IMRT fields. Radiotherapy and Oncology 71, 223–234

38. Warkentin, B. et al., 2003. Dosimetric IMRT verification with a flat-panel EPID. Med. Phys. 30, 3143-3155

39. Winkler, P., Hefner, A., Georg, D., 2005. Dose–response characteristics of an amorphous silicon EPID. Med. Phys. 32, 3095-3105

40. Winkler, P., Georg, D., 2006. An intercomparison of 11 amorphous silicon EPIDs of the same type: implications for portal dosimetry. Phys. Med. Biol. 51,4189-4200

41. Yeboah, C., Pistorius, S., 2000. Monte Carlo studies of the exit photon spectra and dose to a metal/phosphor portal imaging screen. Med. Phys. 27, 330-33